nature materials

SUPPLEMENTARY INFORMATION

https://doi.org/10.1038/s41563-018-0154-x

In the format provided by the authors and unedited.

# Compositional and orientational control in metal halide perovskites of reduced dimensionality

**Rafael Quintero-Bermudez[1], Aryeh Gold-Parker[2,3], Andrew H. Proppe[1,4], Rahim Munir[5], Zhenyu Yang[1], Shana O. Kelley[4,6], Aram Amassian[5], Michael F. Toney[2] and Edward H. Sargent[1]***

[1]Department of Electrical and Computer Engineering, University of Toronto, Toronto, Ontario, Canada. [2]SLAC National Accelerator Laboratory, Menlo Park, CA, USA. [3]Stanford University Department of Chemistry, Stanford, CA, USA. [4]Department of Chemistry, University of Toronto, Toronto, Ontario, Canada. [5]King Abdullah University of Science and Technology (KAUST), KAUST Solar Center (KSC), and Physical Sciences and Engineering Division, Thuwal, Saudi Arabia. [6]Department of Pharmaceutical Sciences, Leslie Dan Faculty of Pharmacy, University of Toronto, Toronto, Ontario, Canada.
*e-mail: ted.sargent@utoronto.ca

Supporting Information for:

# Compositional and orientational control in metal-halide perovskites of reduced dimensionality

*Rafael Quintero-Bermudez[1], Aryeh Gold-Parker[2,3], Andrew H. Proppe[1,4], Rahim Munir[5], Zhenyu Yang[1], Shana O. Kelley[4], Aram Amassian[5], Michael F. Toney[2], Edward H. Sargent[1]**

## Calculating XRD patterns and Structure Factors

X-ray diffraction (XRD) patterns and structure factors were calculated from Crystallographic Information Files (CIFs) by using the 3D atomistic visualizing software Mercury[1] and VESTA[2], respectively. The CIFs were generated by manipulating a 'template' CIF file for n=40 by cutting out perovskite unit cells to reduce the number of layers in a quantum well. The original n=40 unit cell was generated by grafting together methylammonium (MA) lead iodide and phenethylammonium (PEA) iodide unit cells[3,4]. All CIF manipulation was undertaken by means of custom-made scripts in MATLAB. The end result is a CIF describing n perovskite layers capped by PEA bilayers (e.g., n=5 shown in Figure S1), which contains all the information needed to compute XRD patterns (e.g., Figure 1b).

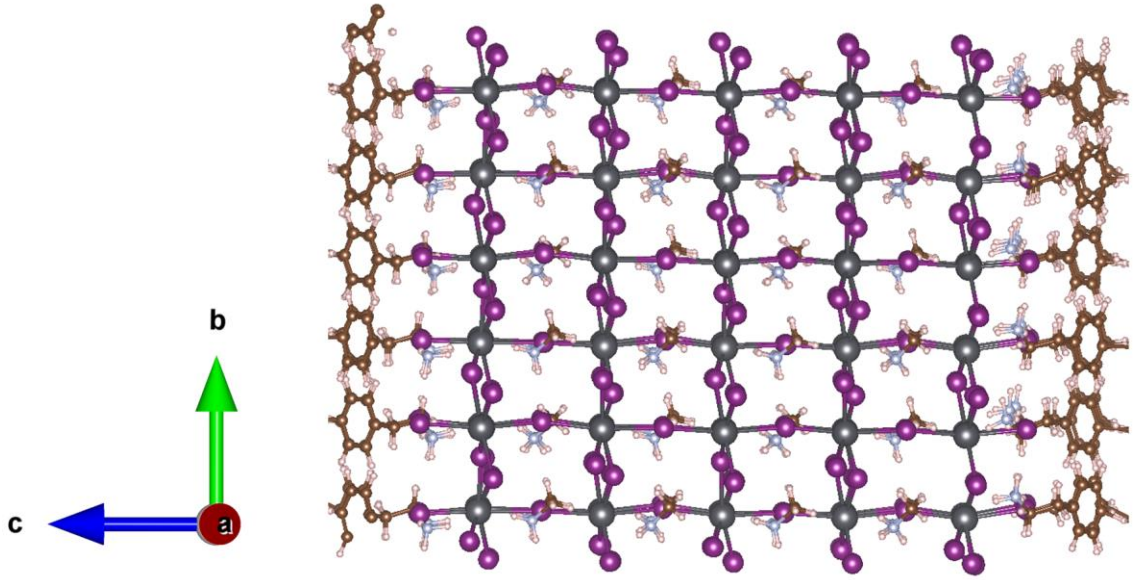


**Figure S1** Unit cell from CIF generated for n = 5 RDP.

## GIWAXS Texture Mapping

2D GIWAXS data can be used to determine the orientation of crystallites in quasi-2D perovskites. The analysis differs for samples in different regimes (classified according to Figure 5). In samples of $1 < \langle n \rangle < 5$, for instance it is easy to identify (00*l*) diffraction peaks for the small wells (Figure S2). In $\langle n \rangle$=2 for instance, the (00*l*) diffraction peaks for n=2 can be observed, each with a tendency to orient with the organic bilayers parallel to the substrate. The GIWAXS data also shows anisotropic rings, which resemble peaks in bulk $MAPbI_3$ (i.e., 3D perovskite). These (hk0) reflections (labelled in white in Figure S2a), corresponding to ordering along the organic bilayers, reflect scattering from the perovskite unit cells within the n = 2 quantum wells.

The intensity as a function of $\chi$ for (110) and $(003)_{n=2}$ reflections corroborate the orientation of the RDPs in this case (Figure S2c). Note the sharp intensity as $q_{xy} \rightarrow 0$, for the (00x) reflections, whereas the (110) peak shows higher intensities as $q_z \rightarrow 0$. The non-negligible intensity for the latter as $q_{xy} \rightarrow 0$ is due to the (002) perovskite diffraction which overlaps with the (110). Furthermore, in Figure S2b it can be observed that diffraction peaks with non-zero *l* values (in (*hkl*) notation of XRD peaks) are broader than those with a zero *l* value (i.e. poor spatial coherence along c axis); further evidence that the rings also identify n=2 wells.

Taken together, the GIWAXS reflects n=2 perovskite with a tendency to orient with the organic bilayers parallel to the substrate, but with a broad distribution centered about this parallel orientation.

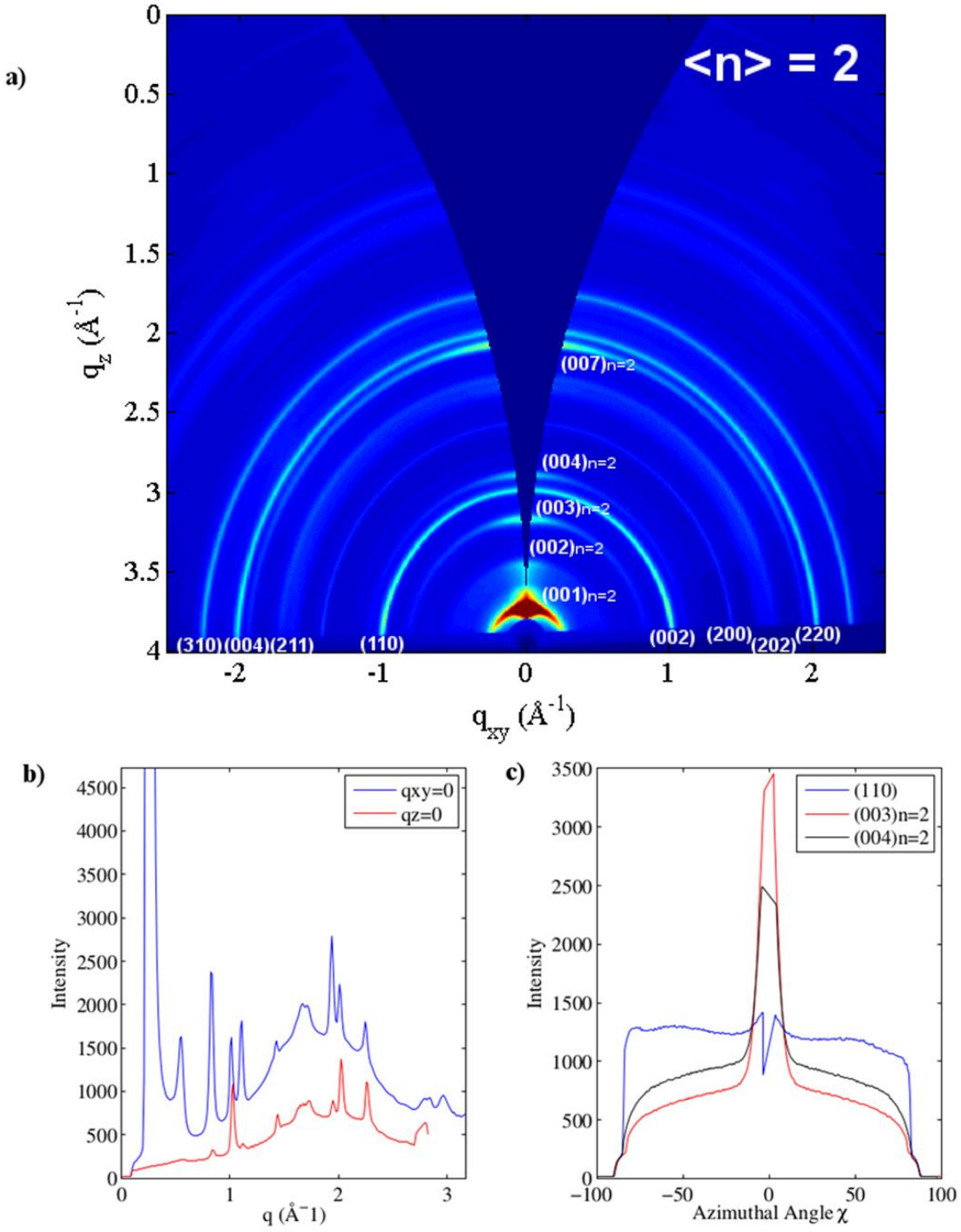


**Figure S2** (a) Labelled GIWAXS pattern of <n> = 2 sample. Pattern is shown before 'missing wedge' correction to facilitate labeling. The plots are displayed with q axes despite being pre-correction to facilitate visual identification of peaks. (b) Pie cuts of 20° extent along vertical and horizontal axes. (c) Intensity as a function of azimuthal angle.

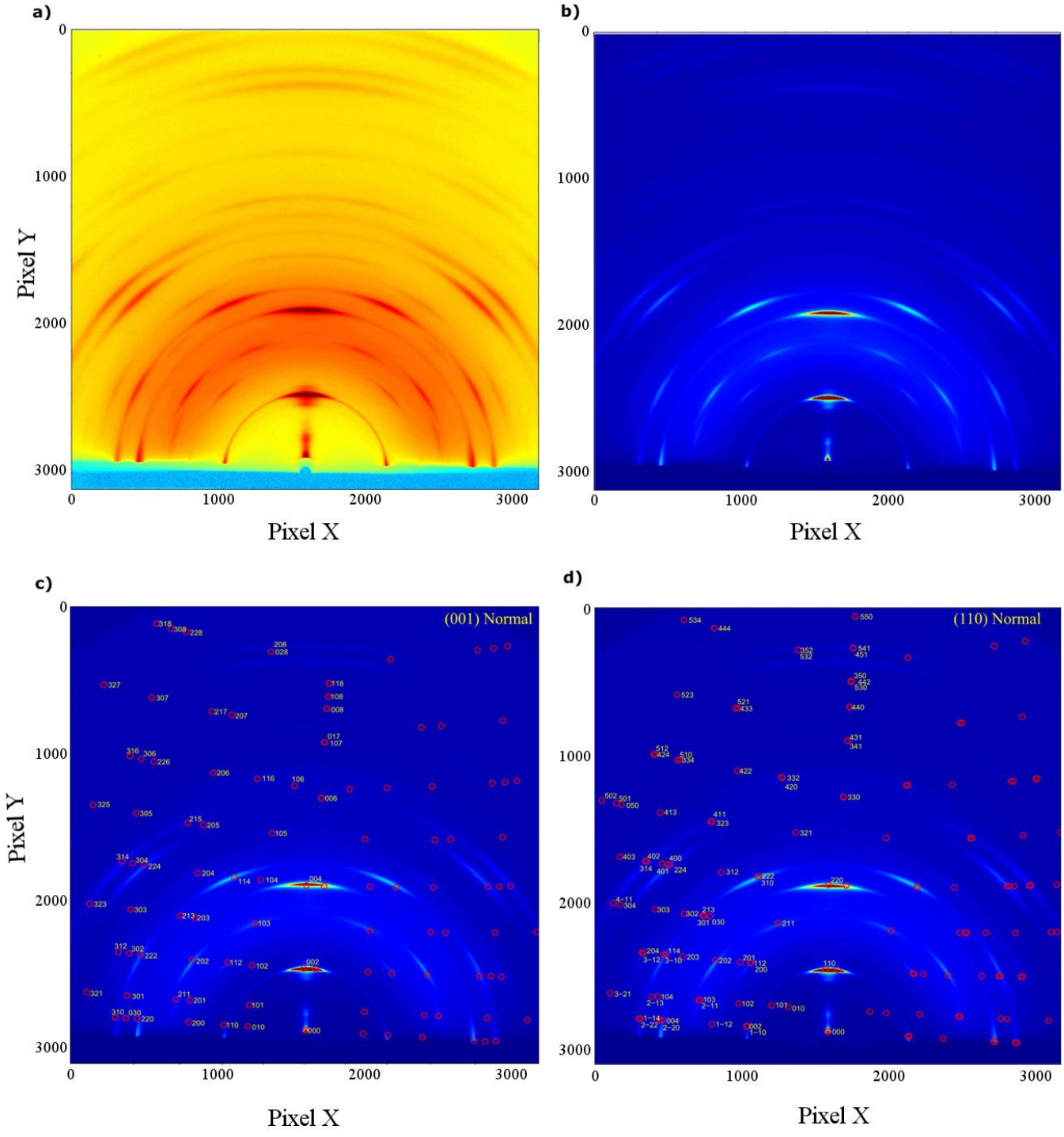


**Figure S3** Texture-mapped GIWAXS results of <n> = 8 sample. Patterns are shown before 'missing wedge' correction to facilitate labeling. Plots for (a) logarithmic color scale, (b) linear color scale, texture mapping for (001) normal to substrate, i.e. horizontal-lying wells (c), and texture mapping for (110) normal to substrate, i.e. vertical-standing wells are shown.

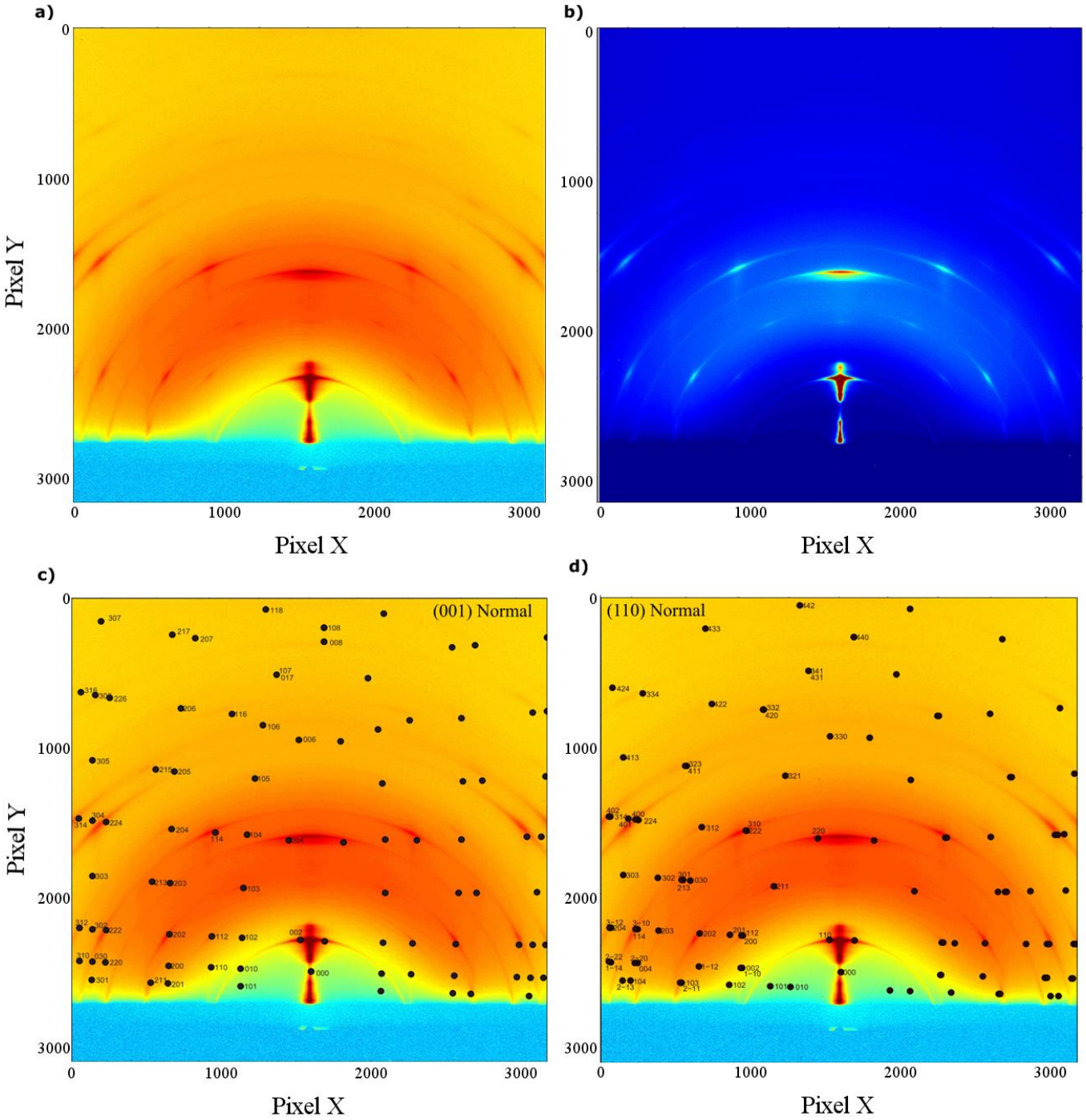


**Figure S4** Texture-mapped GIWAXS of <n> = 5 sample. Patterns are shown before 'missing wedge' correction to facilitate labeling. Plots for (a) logarithmic color scale, (b) linear color scale, texture mapping for (001) normal to substrate, i.e. horizontal-lying wells (c), and texture mapping for (110) normal to substrate, i.e. vertical-standing wells are shown.

2D GIWAXS of $\langle n \rangle > 4$ requires texture mapping with high sensitivity to the q value and angle at which diffraction peaks appear. The analysis must consider all possible crystallite orientations to ensure that there is not a misinterpretation of the GIWAXS pattern. In order to facilitate this analysis, we made use of GIXSGUI's texture mapping features[5]. Figures S3 and S4 show the results of texture mapping for $\langle n \rangle$=5 and $\langle n \rangle$=8 samples assuming that the perovskite unit cell aligns with the (001) surface parallel to the substrate and that the (110) surface is parallel to the substrate. All other surfaces were found to lead to GIWAXS patterns that did not match the experimental patterns.

It is immediately noticeable that the patterns displayed by these two alignments (110 parallel) and (100 parallel) are very similar. It is only with thorough analysis that one can discern the alignment of the crystallites in our quasi-2D films. The clearest peak that can be used to differentiate these two alignments is that at q=1.6 $Å^{-1}$ (due to (211) and (103) in the tetragonal unit cell, Figure S5). (001) alignment should exhibit peaks at both ~20$^o$ and ~75$^o$ along the azimuthal angle, but the peak at ~20$^o$ corresponding to the (103) diffraction has a structure factor that is orders of magnitude weaker than that of the stronger (211) peak at ~75$^o$. A (110) alignment (with the organic bilayers perpendicular to the substrate) however, exhibits (211) peaks at both ~20$^o$ and ~75$^o$, matching the observed patterns for both $\langle n \rangle$=5 and 8. Furthermore, this alignment can be discerned to some degree in samples with very large wells (e.g. $\langle n \rangle$=40 in Figure S7). The distribution of quantum well thicknesses can be corroborated with transient-absorption spectroscopy (TAS) (Figure 2) to ensure that no misinterpretations have taken place.

Therefore, we can confidently affirm that large wells ($\langle n \rangle > 4$) preferentially orient with the large organic bilayers perpendicular to the substrate.

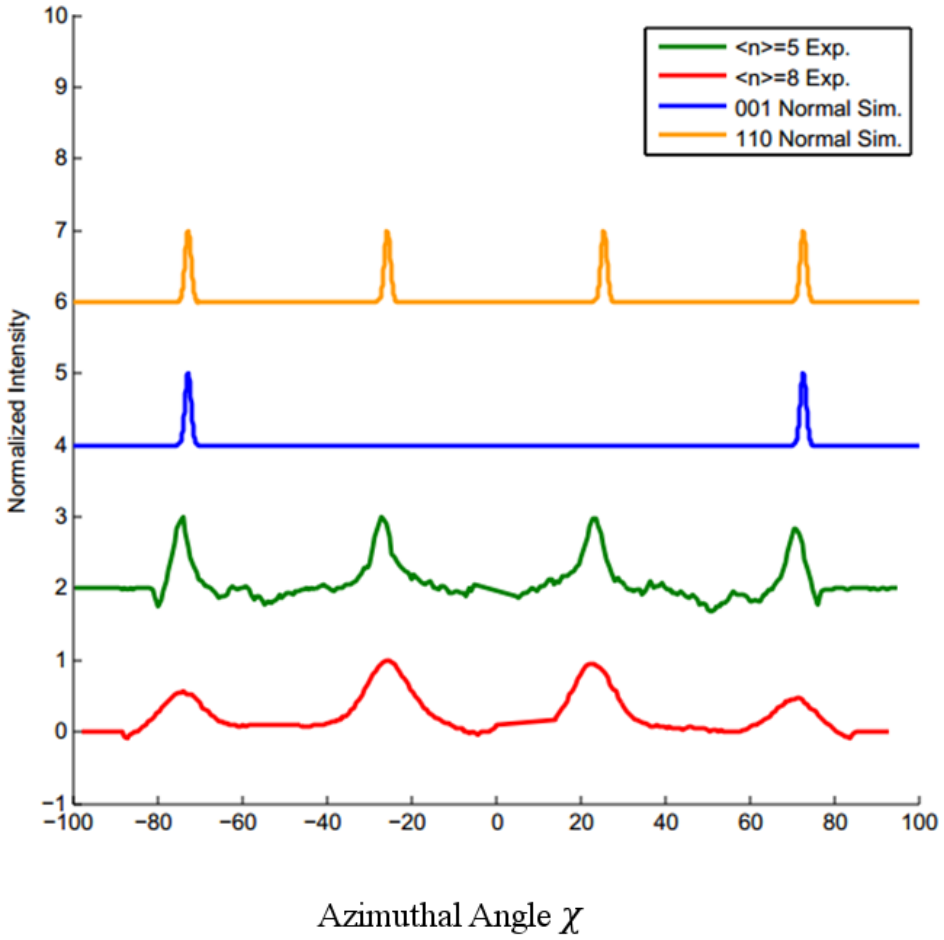


**Figure S5** Intensity as a function of azimuthal angle for q = 1.6 Å$^{-1}$.

## The importance of spatial coherence for XRD peaks

The intensity and width of an XRD peak will depend on the crystallinity or spatial coherence of the given ordered domain. In RDPs, the (001) diffraction peak of a given QW will be determined by its ordered domain's spatial coherence. For instance, the peak width and intensity of an n=4 peak will vary depending on whether the ordered region is composed of 4 identical adjacent n=4 QWs (high intensity and narrow peak) or of a random mix of QWs (low intensity and broad peak) including a few of n=4 (Figure S6).

The size of a coherently diffracting region (i.e. grain) can be determined from an XRD peak by means of the Scherrer equation:

$$l = \frac{K\lambda}{\gamma cos\theta},$$

where K, λ, γ, and θ are the form factor, X-ray wavelength, FWHM (after instrumentation broadening has been subtracted out) and diffraction theta (i.e., half of 2θ) of a peak used to determine crystallite size[6].

Therefore if a grain is made up of a random assembly of quantum wells or does not exhibit enough repetitions of the same QW, it will exhibit a weak and broad XRD peak. Both causes listed are enhanced in large-n quantum wells, given the decreased probability in forming a large-n grain (Figure 4a) and the increased dimensions necessitated by a large-n grain (e.g., 5 repetitions of n=10 is about 40nm). The measured GISAXS patterns are therefore fully consistent with the other characterizations (including TA) and the morphology (Figure 5e-f). To be specific, the $\langle n \rangle$=5 and 10 samples exhibit an increase in the baseline scattering with respect to the bulk sample, consistent with broad XRD scattering for large-n wells in this region. Furthermore, the asymmetry in the n=3 peak in the $\langle n \rangle$=5 sample suggests the presence of other QW sizes, n=4 for instance.

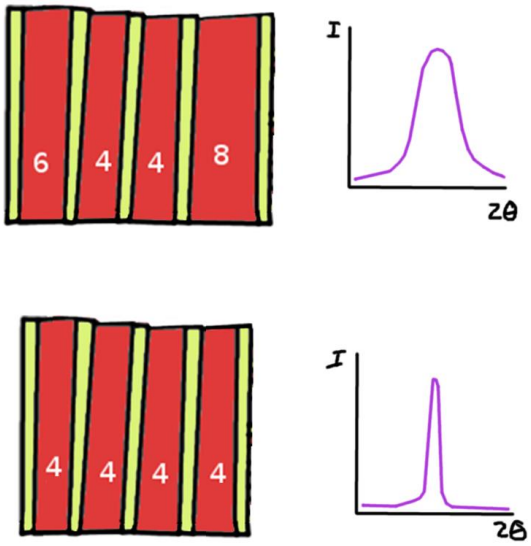


**Figure S6** Random assembly of large-n wells.

## Calculating probability distributions

With the aid of the formation kinetics model (Figure 3d), we are able to calculate the probability distribution of wells for a given ⟨n⟩ value. The ratio of large cations to the intermediate solvent complexes can be seen as the defining parameter behind the probability distribution for different QW thicknesses. Since ammonium salts are highly soluble in DMSO, we simplify the model by assuming that large cations are homogeneously distributed throughout the as-deposited film (i.e. not annealed). Furthermore, excess DMSO is provided in the synthesis to ensure homogenous precursor distribution and that solvent does not limit kinetics. The model therefore assumes that the probability of forming a well of a given size is constant throughout the film. Statistics of well

formation can be computed analytically as permutations with repetition. In order to account for variation in the local concentration of the large cation during the growth of RDP, we also developed a Monte Carlo simulation to verify the validity of our assumption (details in following section).

It is instructive to verify independently the findings of Figure 1b-d by computing the probability of forming a single well of size n (in a given film ⟨n⟩) and compare to the probability of forming a highly crystalline domain with well size n that would exhibit a strong distinct XRD signal (Figure 4a). For this analysis a crystallite domain is defined as an ensemble of 5 identical QWs. This analysis finds that it is drastically less probable to form an entire domain of a given well thickness than it is to form a single well. Furthermore, this probability decreases significantly with well size such that an entire grain of n>5 is highly unlikely. This finding reconciles the results from GISAXS (Figure 1c) and TA (Figure 2) such that despite the abundant presence of large QWs, poor spatial coherence for large QWs will lead to broad weak diffraction peaks that merge together as observed in the scattering < 2 $nm^{-1}$.

The distribution of well thicknesses n in film ⟨n⟩, can also be computed with the model (Figure 4b). The simplified analytical expression finds a skew lognormal distribution. A Monte Carlo simulation which does not assume constant large cation distribution over time agrees with the analytical expression for large n values; however, this more intricate model leads to a correction in the distribution for thin wells leading to a symmetric lognormal distribution. The adjustment is expected since a depletion in large cation inhibits the formation of very thin wells. For large wells, however, the analytical expression matches the Monte Carlo simulation, i.e., the assumptions in the analytical expression are justifiable in this range.

The statistical simulation exhibits a lognormal well thickness distribution, denoting a tighter standard deviation for low-n wells than large-n wells. The peak of the distribution is closely centered on the ⟨n⟩ value, but the distribution extends to larger wells, a property inherent to lognormal distributions. The average well thickness is thus just greater than the ⟨n⟩ value. This result agrees well with all other measurements, notably ultrafast TA where the bleach signals identify the QW thickness distribution in the film, with one glaring exception.

Large bleach peaks for low n wells are observed in TA that do not follow the lognormal distribution (particularly among spin-cast films). It was mentioned in the manuscript that this could result from variations in oscillator strength; or due to the positive red-shifted spectral feature exhibited by pure QWs. An inhomogeneous distribution of the dissolved large cation throughout the film could also lead to this departure from a lognormal distribution of well thicknesses. This phenomenon could also explain the aforementioned variation in well sizes from top to bottom of the film. In order to isolate these effects, various spectra were collected for the same sample to determine the variation of bleach intensities (Figure S24, Table ST1). Upon quantifying the variation in bleach intensities across the film for different n values, we concluded that each effect takes place, yet the effect of the inhomogeneous distribution of QWs is quantitatively smaller. The increase in bleach discussed here is mainly observable in QWs of n= 2 and 3.

Under the assumption of a homogeneous distribution of dissolved intercalating cation (PEA in this case), the probability of forming a single quantum well or a perfect grain (i.e., 5 repeating identical quantum wells) can be calculated as permutations with repetition. There is a fixed probability throughout the film of forming a PEAI bilayer at a given stage of the growth (Figure S7). In figure S7 for instance, there is a probability that the next layer grown will be a PEAI layer and the remainder probability that it will be another PbI6 layer. The probability for these is set by the ratio of PEAI to all other precursors used in the initial solution, such that the probability of a new PEAI layer at a given site in a sample $\langle n \rangle$ is:

$$\rho \propto \frac{1}{\langle n \rangle},$$

assuming that the precursor ratio and distribution are the primary factors determining the probability, the proportionality sign can be replaced for an equality and the probability of getting a well of size n in a sample $\langle n \rangle$ can be found by:

$$P_n = (\rho)(1-\rho)^{n-1}(\rho)n = \left(\frac{1}{\langle n \rangle}\right)^2 \left(1 - \frac{1}{\langle n \rangle}\right)^{n-1} n\,.$$

The probability distributions in Figure 4b were further normalized by taking into account the total mass difference in different-sized wells.

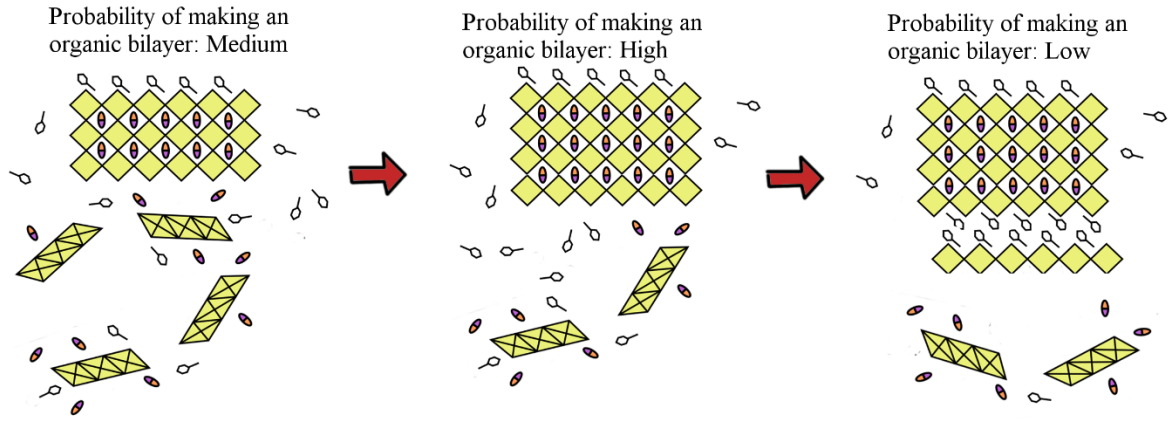


**Figure S7** Probability model for forming quantum wells. As soon as an organic bilayer is formed, the PEA around the growing RDP is used up temporarily depleting the distribution. As a result, the probability of forming an organic bilayer is much lower momentarily. As the RDP continues to grow, the local distribution of PEA goes back to normal due to diffusion. The Monte Carlo takes this phenomenon into account thereby correcting the simpler analytical model.

## Monte Carlo Simulation

A Monte Carlo simulation was developed to account for variations in the distribution of large cation throughout the film during the process of RDP growth. As RDPs grow, there is a point in time when there is sufficient dissolved large cation to nucleate an organic bilayer. At this point the availability of the large cation is temporarily depleted around the growing RDP. This would mean that the actual growth of RDPs would lead to a distorted distribution compared to the analytically computed populations (see calculating probability distributions).

In order to account for the variation in large cation during RDP growth, we chose to statistically simulate the growth process by fixing the probability of forming an organic bilayer (the probability of which is set by the ratio of PEAI to all other precursors). Once an organic bilayer is formed we temporarily reduce the probability of forming an organic layer and slowly increase it as further perovskite monolayers are formed.

The rate at which the probability returns back to normal was varied in order to calibrate this value. The specific rate, however, was not found to alter the resulting distributions on Figure 4b significantly.

## Determining bandgap of RDPs

In order to predict the size-dependent bandgap of RDP quantum wells, we identified the ultrafast TAS bleach wavelength for each distinguishable RDP quantum well feature (all wells $n \leq 5$ can be distinctly discerned), and the bulk perovskite bleach. These energy values were plotted and compared to the bandgap of these materials reported in previous literature[7–9] to ensure that the results agree with each other (Figure S8a). Using a method similar to that of Moreels *et al.*, we used our data points to fit a predicted bandgap dependence on nanostructure size[10]. In this case, we fitted to a function of the form: $E_0 = E_g + \frac{1}{0.25d^2+0.25d+1.038}$, where the last term in the denominator is added in order to reduce the slope of the function for small thickness values. In order to validate our empirical fitting, we corroborated our predictions by means of an effective-mass-approximation (EMA) model[11] (Figure S8a). The EMA model finds, as expected, an agreement with the empirical fitting near the exciton Bohr radius[12], but deviates at very small quantum well thickness values (due to the size-dependent Coulomb interaction among other features that become prominent in very strong confinement)[11].

Confident in our predictive empirical fitting, we compute the predicted bandgap alongside the bulk bandgap of $MAPbI_3$ perovskite (Figure S8b). The ultrafast TAS bleach is expected to exhibit blue-shifted features in both quantum confined and bulk-like perovskite materials due to strong exciton-exciton interactions[7] and Moss-Burnstein phenomena[13], respectively. This blue-shift is determined experimentally by means of our TAS data and used to compute the predicted ultrafast TAS bleach. This analysis is by no means expected to provide an infallible bandgap value for each RDP quantum well size, but instead meant to provide a good estimate for identifying TAS features in Figure 2.

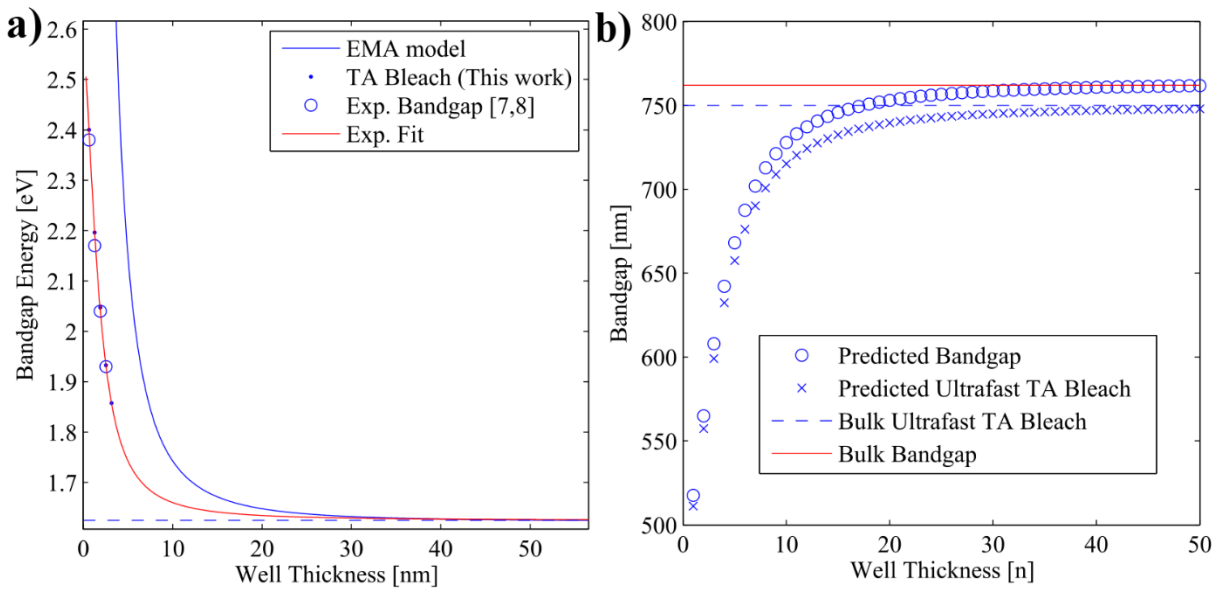


**Figure S8** Predicted bandgap and ultrafast TAS bleach of RDPs of varying thickness

## Fitting Ultrafast Spectra

The UTA spectra at 3 ps exhibits the bleach for all excited QWs before charge transfer has taken place. As such, it is possible to identify the distribution of QW thicknesses present in the RDP film. In order to quantify this population (Figure S9), the spectra are fit to a sum of Gaussian waveforms centered at the wavelengths determined in the previous section (Figure S8b). Individual Gaussians are used for n = 1 to 12. For higher n values Gaussian waveforms are used to represent groups of QWs due to their close energetic spacing. That is, one Gaussian for n = 12 to 15, 15 to 20, 20 to 30 and 30 to 40. Above n = 40, the bandgap is too close to distinguish from a bulk bleach.

For the fitting, linewidths are fit for n = 1 to 5 and for the bulk bleach. For all other n values, the linewidth used is interpolated between that acquired for n = 5 and bulk, as it is expected that the bleach will broaden as quantum confinement is weakened. In addition a broad band positive Gaussian waveform is used to fit the positive blue feature, which has been previously attributed to exciton-exciton interactions[7].

It is important to specify that the fitting determines the distribution of bleach intensities. This can help ascertain which QW thicknesses are exhibited in a particular film, but does not necessarily imply the actual QW thickness distribution. There are two reasons for this: (1) varying oscillator strengths for different n values, where the oscillator strength is expected to increase an n decreases, (2) the red positive feature identified in pure single crystals would inhibit the total bleach observed for the next higher-n valued QW.

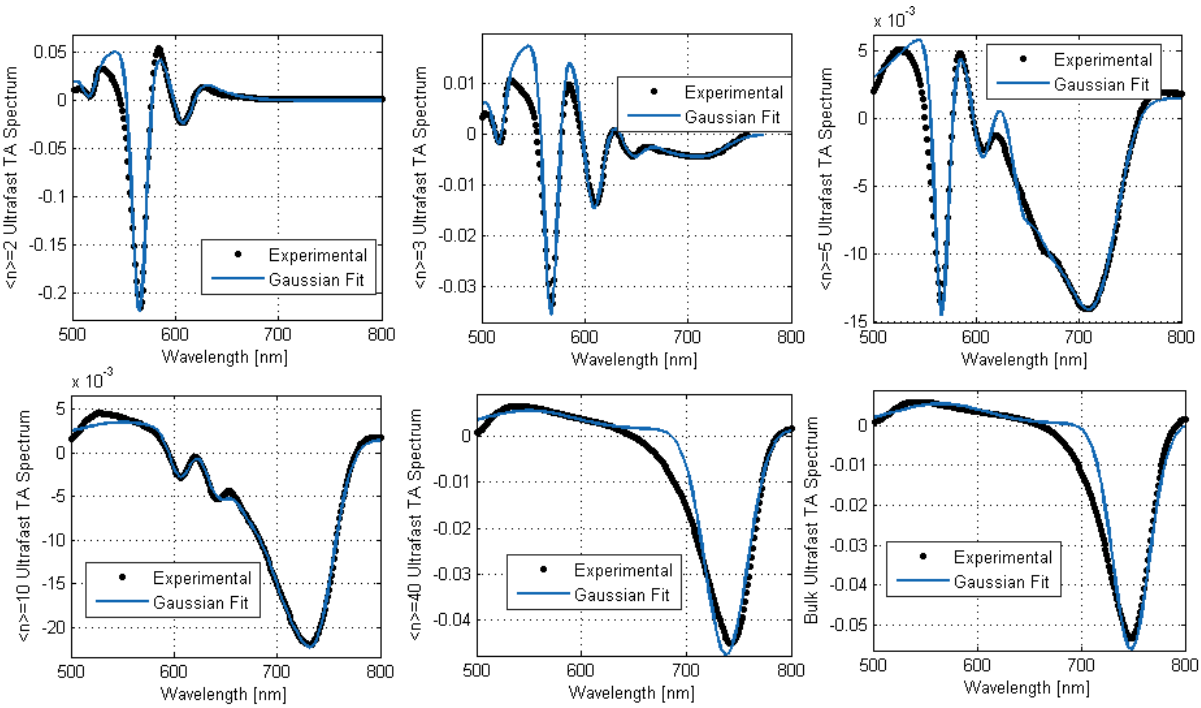


**Figure S9** Fitting of the UTAS spectra for various n values with a sum of Gaussian waveforms centered at the wavelengths determined by EMA (Figure 2l).

## Supporting Figures & Tables

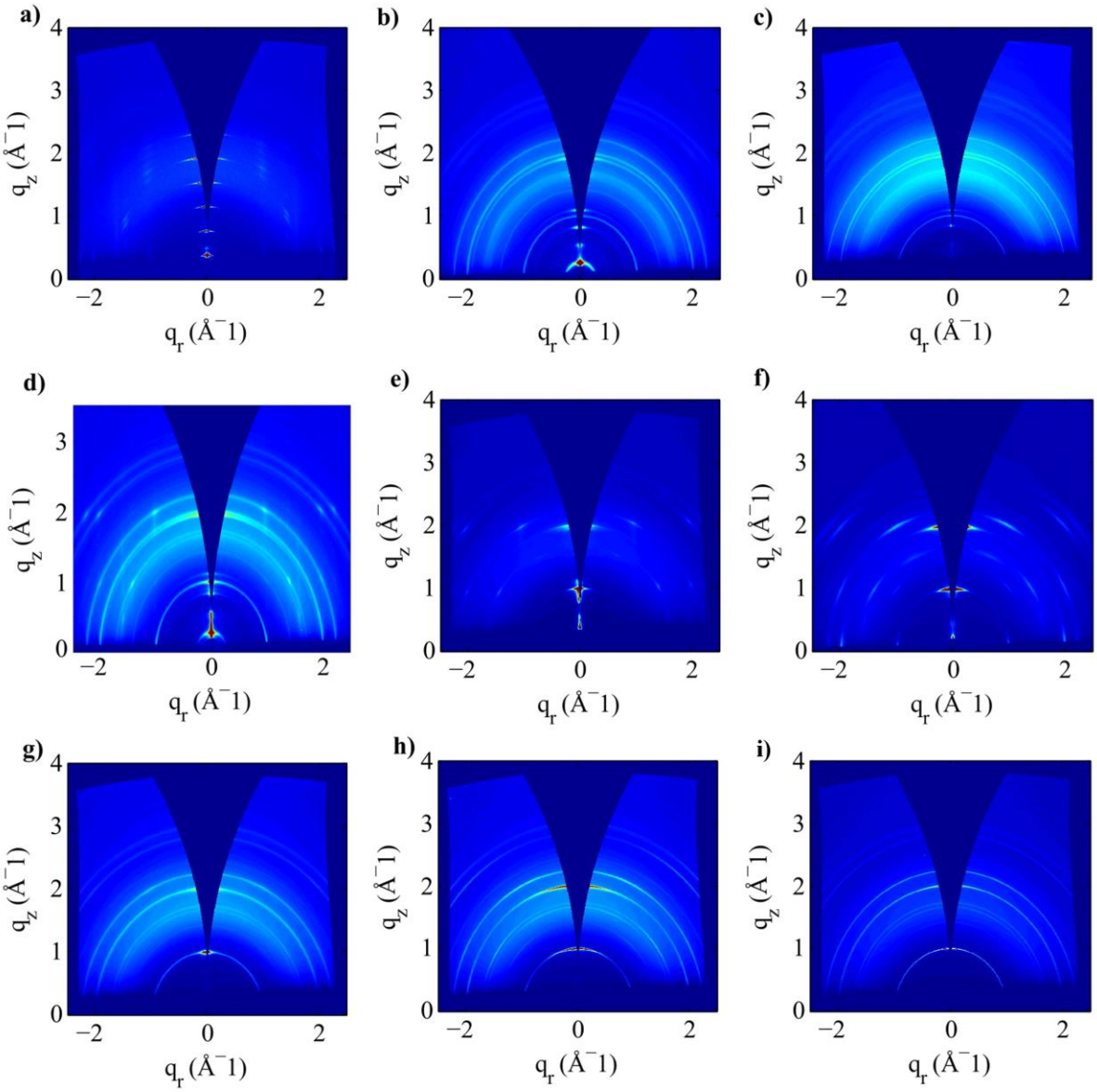


**Figure S10** GIWAXS results of PEA-$MAPbI_3$ samples <n> = 1 (a), 2 (b), 3 (c), 4 (d), 5 (e), 8(f), 10 (g), 40 (h) and bulk (i) on glass substrates.

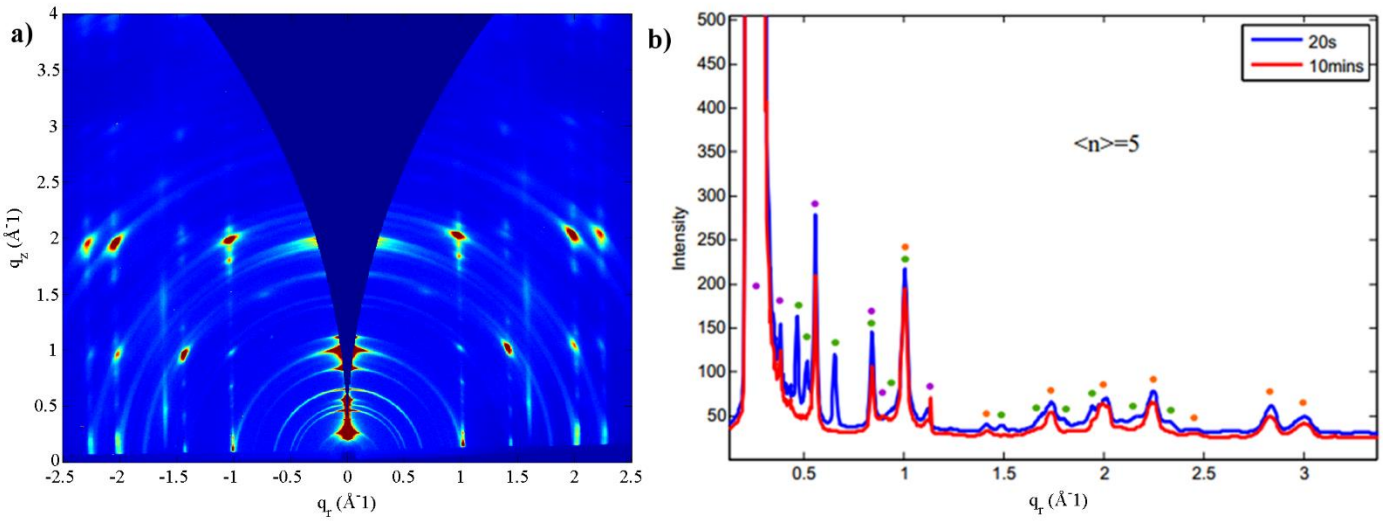


**Figure S11** In-situ GIWAXS results of sample <n>=5. Pattern at 20s (a) and integrated patterns at 20 s and 10 mins (b).

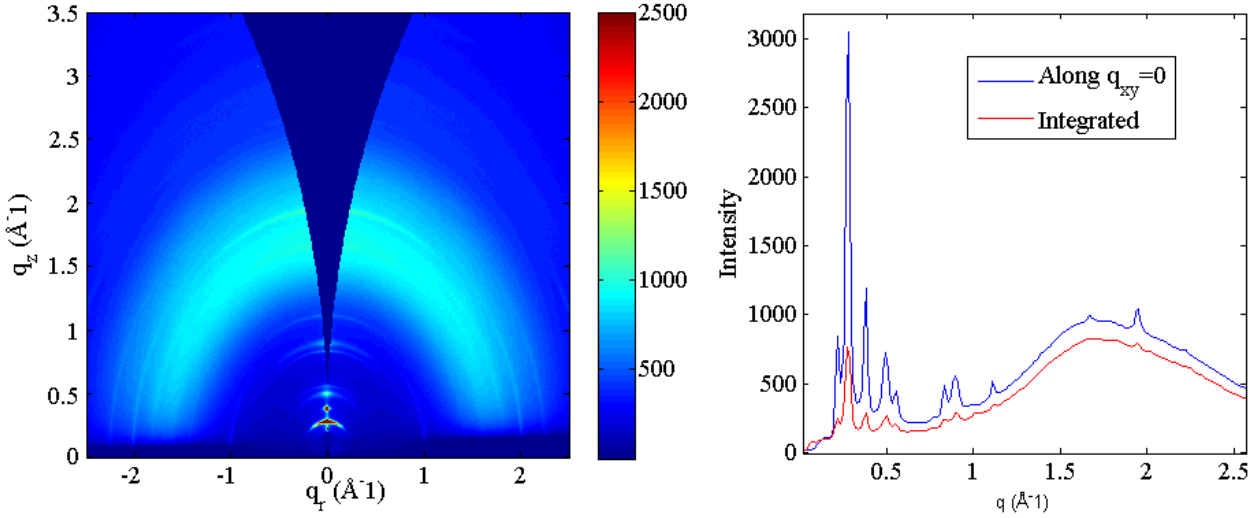


**Figure S12** GIWAXS pattern for thin film <n>=5. Thickness is approximately 50 nm, measured by AFM. This is compared to the patterns on Figure S10 (in this case S10e) which is measured on films of approximately 200 nm.

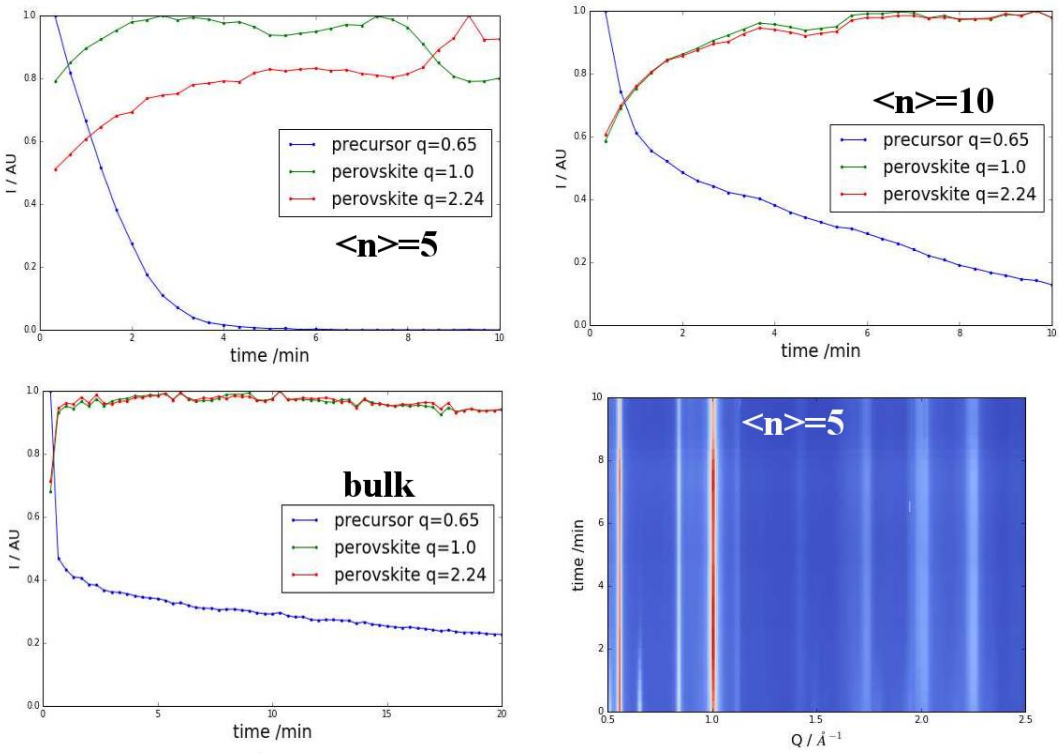


**Figure S13** Kinetics analysis in RDP films and bulk demonstrates slower kinetics as <n> increases. Bottom right is a waterfall plot integrating all in-situ data in <n>=5 during annealing.

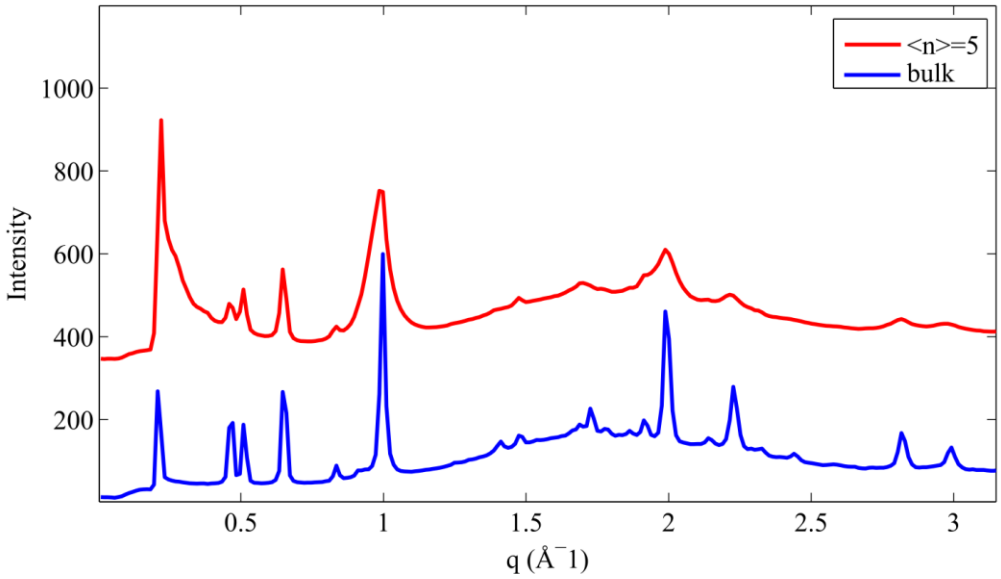


**Figure S14** Pre-annealed GIWAXS cuts (along $q_z$ axis) of <n>=5 film and bulk film reveal the same patterns indicating that PEAI does not participate in the pre-annealed intermediate complexes.

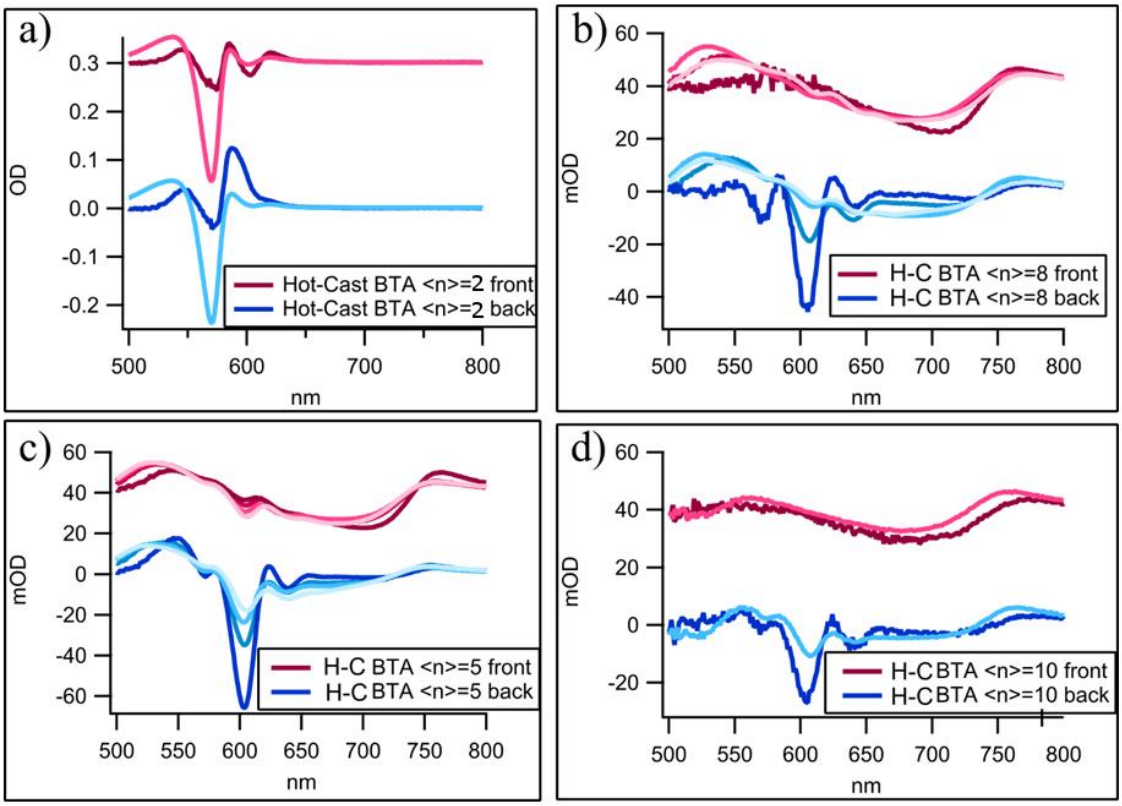


**Figure S15** TAS on Hot-Casted samples with BTA as the large cation. Measurements show spectra upon front and back pump excitation revealing the difference in QW population throughout the sample thickness. The thickness of the sample is varied from 50 to 300 nm showing more dramatic trends for thicker films (effectuated by the molar ratio in the solution). The darkest trace represents the thickest sample and the lightest trace, the thinnest sample.

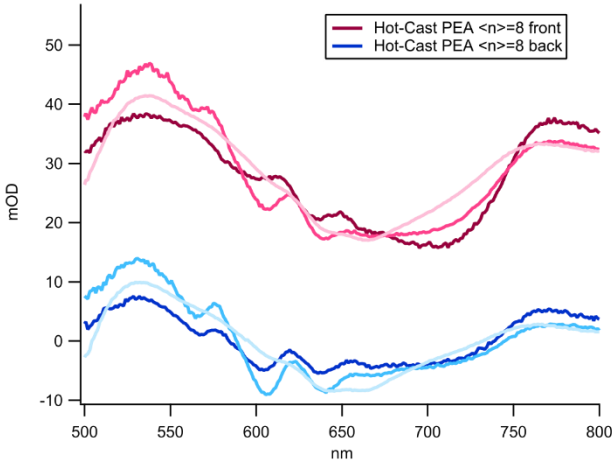


**Figure S16** TAS on Hot-Casted samples with PEA as the large cation. Measurements show spectra upon front and back pump excitation revealing the difference in QW population throughout the sample thickness. The thickness of the sample is varied from 50 to 300 nm.

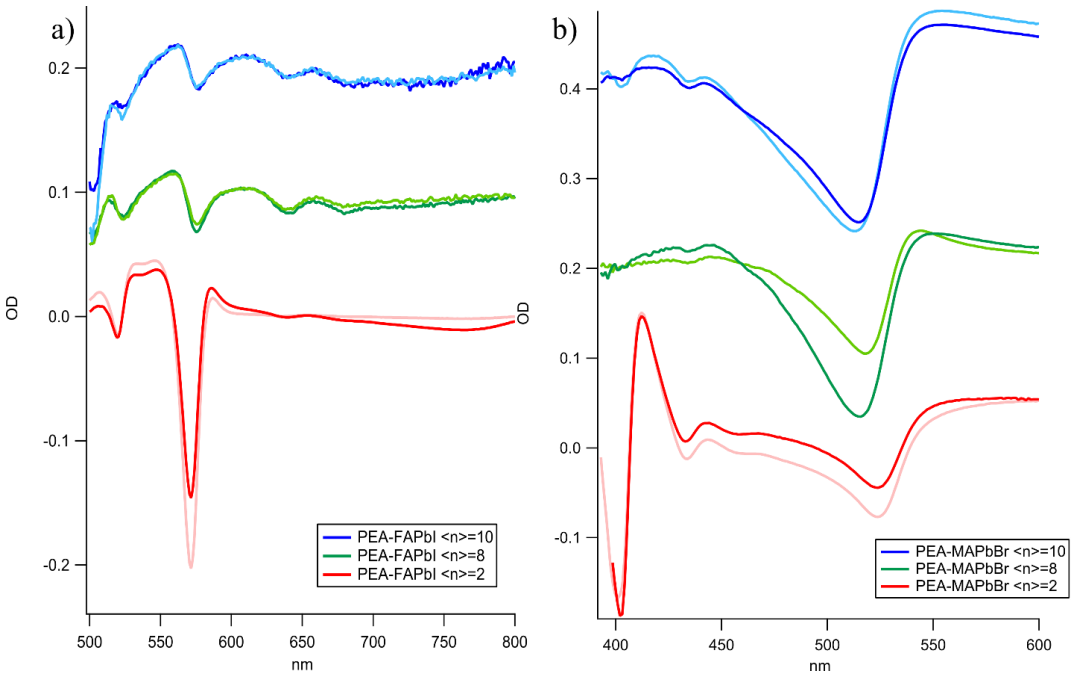


**Figure S17** TAS on normal spin-casted samples with variations in the perovskite crystal (FA and Br). Measurements show spectra upon front and back pump excitation (dark-front excitation, light-back excitation).

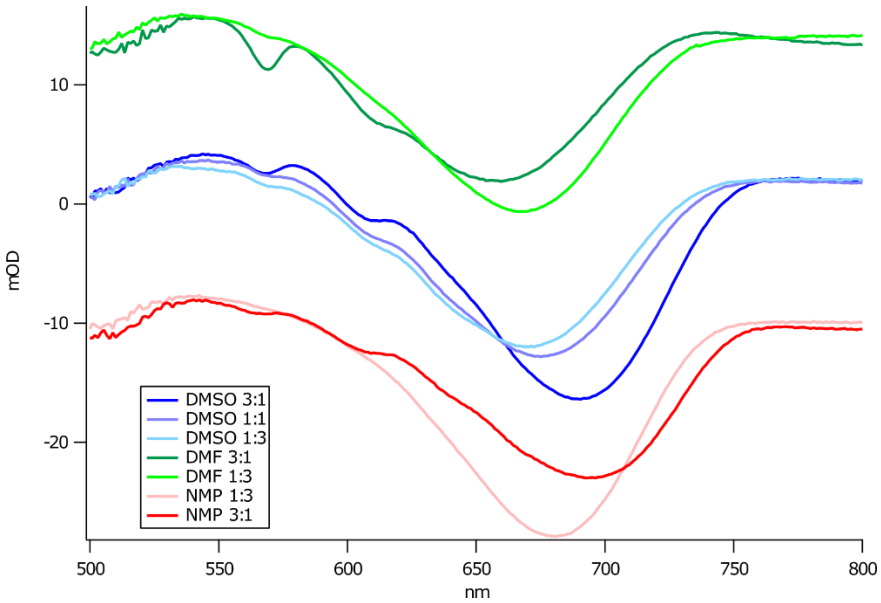


**Figure S18** TAS on normal spin-casted samples with variations in the solvent. The solvent in these cases is composed of GBL and X (where X is either DMSO, DMF or NMP). The ratio was calculated with respect to the sum of all perovskite precursor ingredients. For instance, DMSO 1:3 means 1 part DMSO for every 3 parts of perovskite precursor. Measurements show spectra upon front and back pump excitation (dark-front excitation, light-back excitation). All samples are PEA-MAPbI$_3$ of <n>=5 deposited by spin-casting.

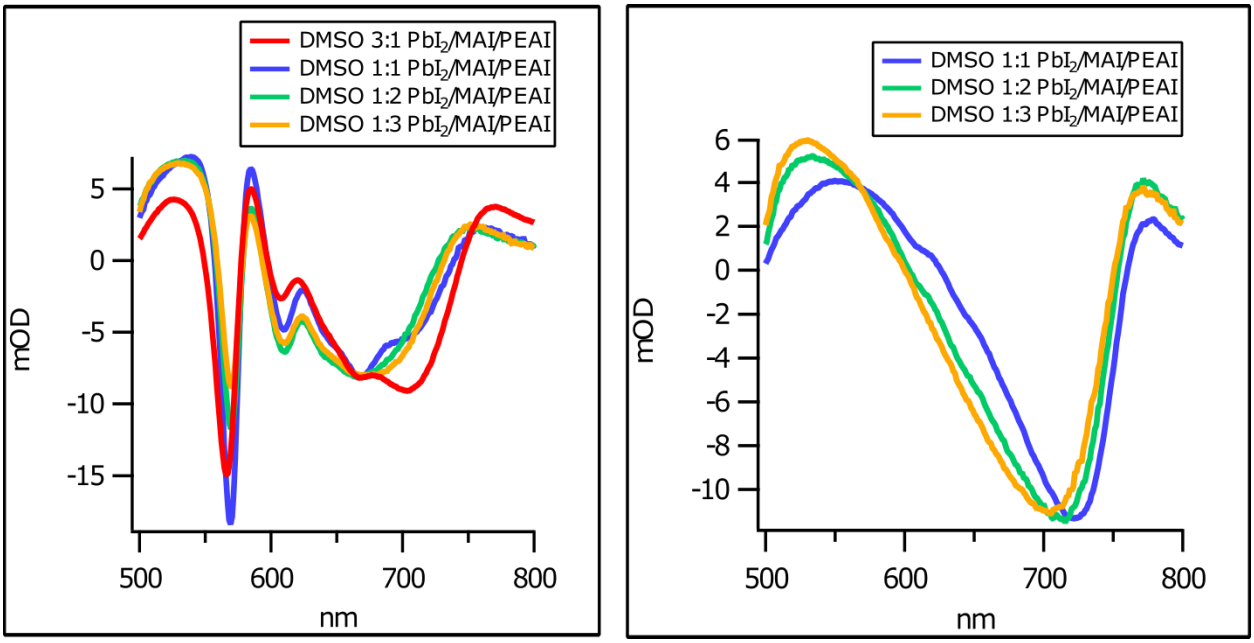


**Figure S19** TAS on normal spin-casted samples with variations in the solvent ratio. The solvent in these cases is composed of GBL and DMSO. The ratio was calculated with respect to the sum of all perovskite precursor ingredients. Samples are PEA-$MAPbI_3$ deposited by spin-casting of <n>=5 (on left) and <n>=10 (on right).

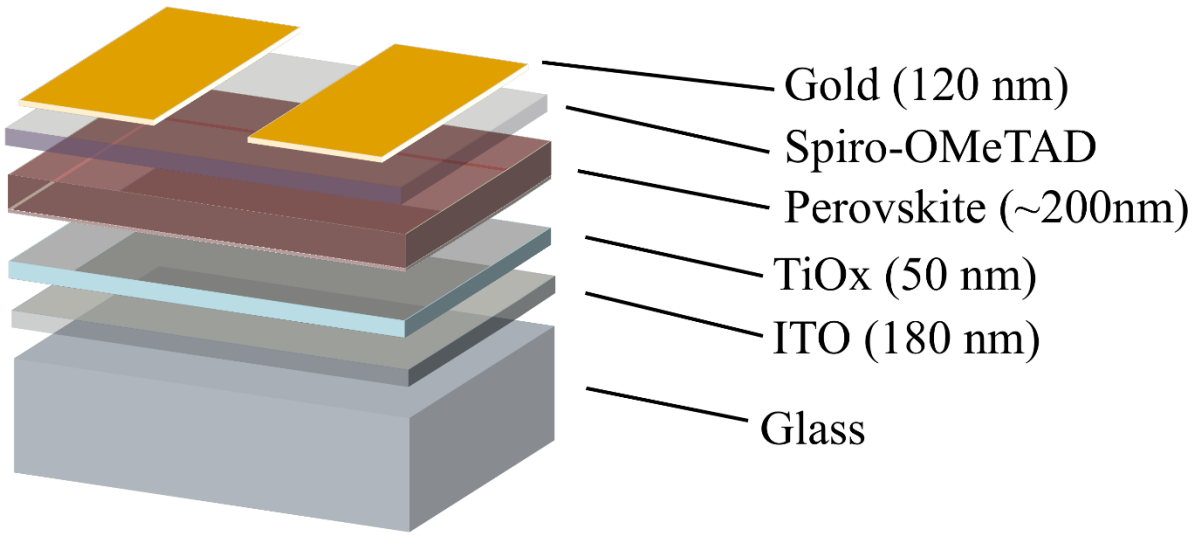


**Figure S20** Architecture of solar cells in this work.

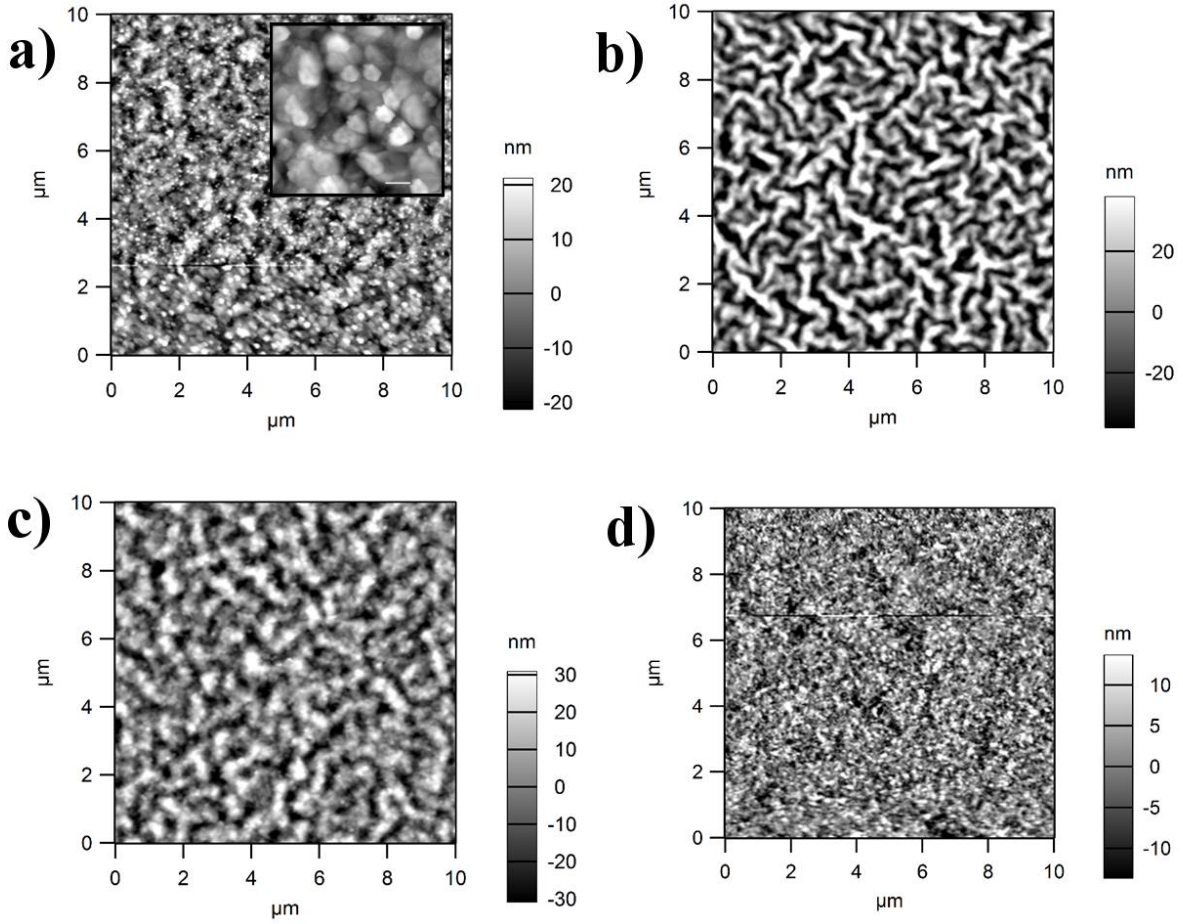


**Figure S21** AFM of PEA-based spin-casting samples <n> = 2 (a), 5 (b), 40 (c) and bulk (d). Inset in (a) shows zoom-in scan of <n>=2 (scale bar: 200 nm). We observe that films of low ⟨n⟩ (such as ⟨n⟩ = 2) formed plate-like grains parallel to the substrate, whereas bulk perovskite films produce grains of various shapes, sizes and orientations. Films of ⟨n⟩ = 5 and larger however, produced corrugated structures resembling that of perpendicularly aligned configurations of other material systems[14,15]. This further confirms the GIWAXS observations that thicker wells (n>3) tend to align normal to the substrate.

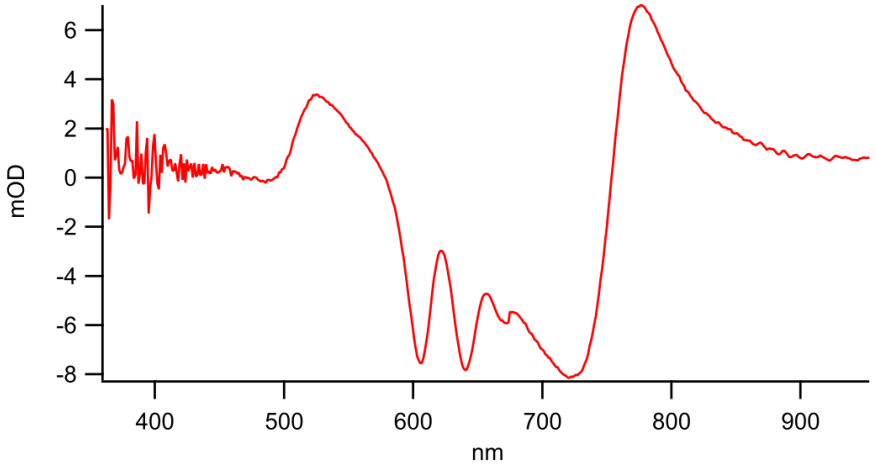


**Figure S22** TAS of sample <n> = 10 showing distinct peaks for n = 3, 4 and 5 RDP components.

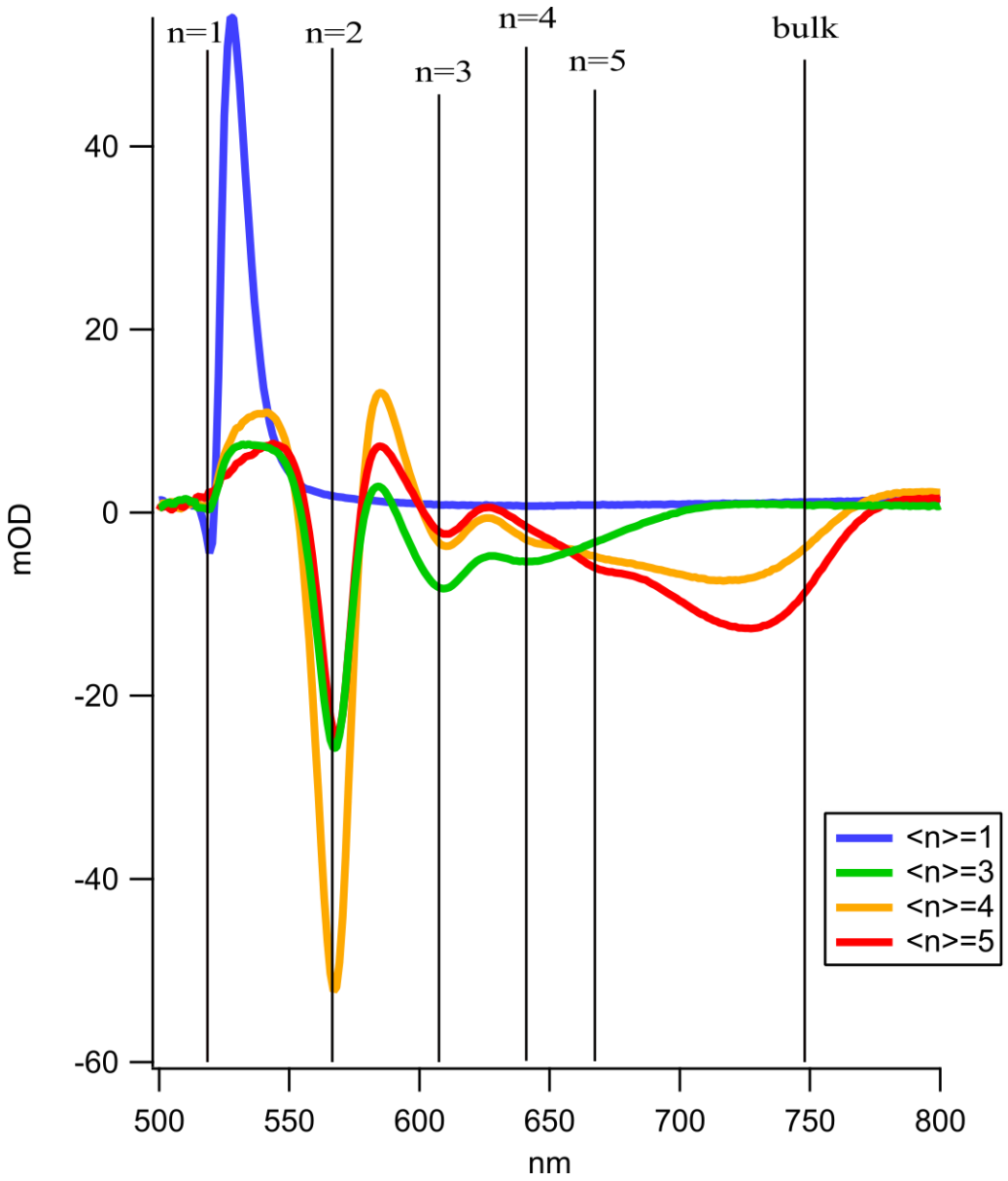


**Figure S23** TAS of PEA-based spin-casting samples with <n>=1-5.

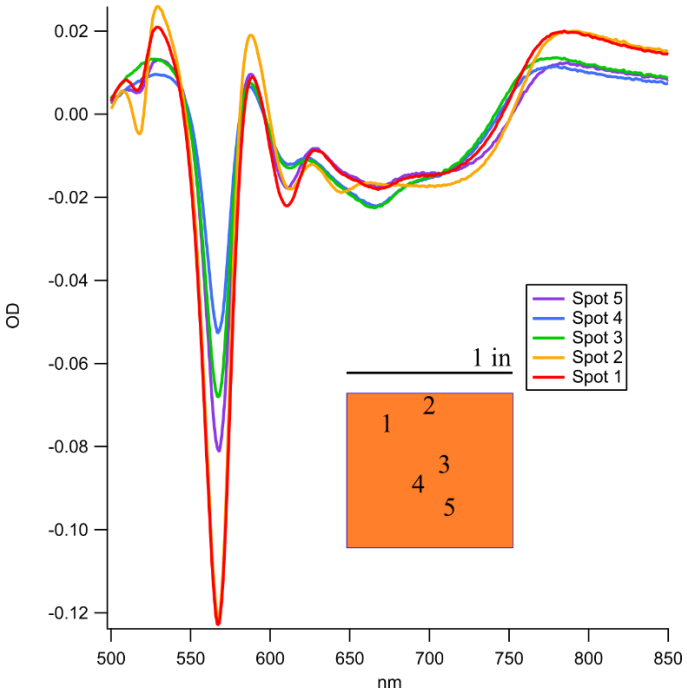


**Figure S24** Various TAS measurements on same sample <n>=5 at various spots on film (depicted in inset). Discrepancies between TA spectra and the modelled lognormal distribution were attributed to variations in oscillator strength; or due to the positive red-shifted spectral feature exhibited by pure QWs. An inhomogeneous distribution of the dissolved large cation throughout the film could also lead to this departure from a lognormal distribution of well thicknesses. In order to isolate these effects, various spectra were collected for the same sample to determine the variation of bleach intensities. Upon quantifying the variation in bleach intensities across the film for different n values, we concluded that each effect takes place, yet the effect of the inhomogeneous distribution of QWs is quantitatively smaller. The increase in bleach discussed here is mainly observable in QWs of n= 2 and 3.

**Table ST1** Summarized data from Figure S17 including bleach intensity at n=2, n=3 and at 700nm. Data in last 3 columns represents bleach intensities normalized to the median values. Standard deviation for n=2 raw data is about 1 order of magnitude larger than that of neighboring columns, whereas normalized standard deviation values differ by much less. This data suggests that magnitude of n=2 bleach peak is primarily due to increased oscillator strength, whereas small deviations are still discernable (last three columns) evidencing minor variations in population. Larger QWs (n>3) exhibit some differences but the oscillator strength is unlikely to distort observed populations in this range.

| | n=2 bleach | n=3 bleach | 700nmBleach | n=2 Norm | n=3 Norm | 700nm Norm |
|---|---|---|---|---|---|---|
| Spot 1 | .123 | .022 | .014 | 1.54 | 1.22 | 1 |
| Spot 2 | .122 | .018 | .017 | 1.53 | 1 | 1.2 |
| Spot 3 | .068 | .013 | .014 | 0.85 | .72 | 1 |
| Spot 4 | .052 | .012 | .014 | 0.65 | .67 | 1 |
| Spot 5 | .08 | .018 | .014 | 1 | 1 | 1 |
| St. Dev. | .0322 | 0.0041 | 0.0013 | 0.4 | 0.23 | 0.09 |

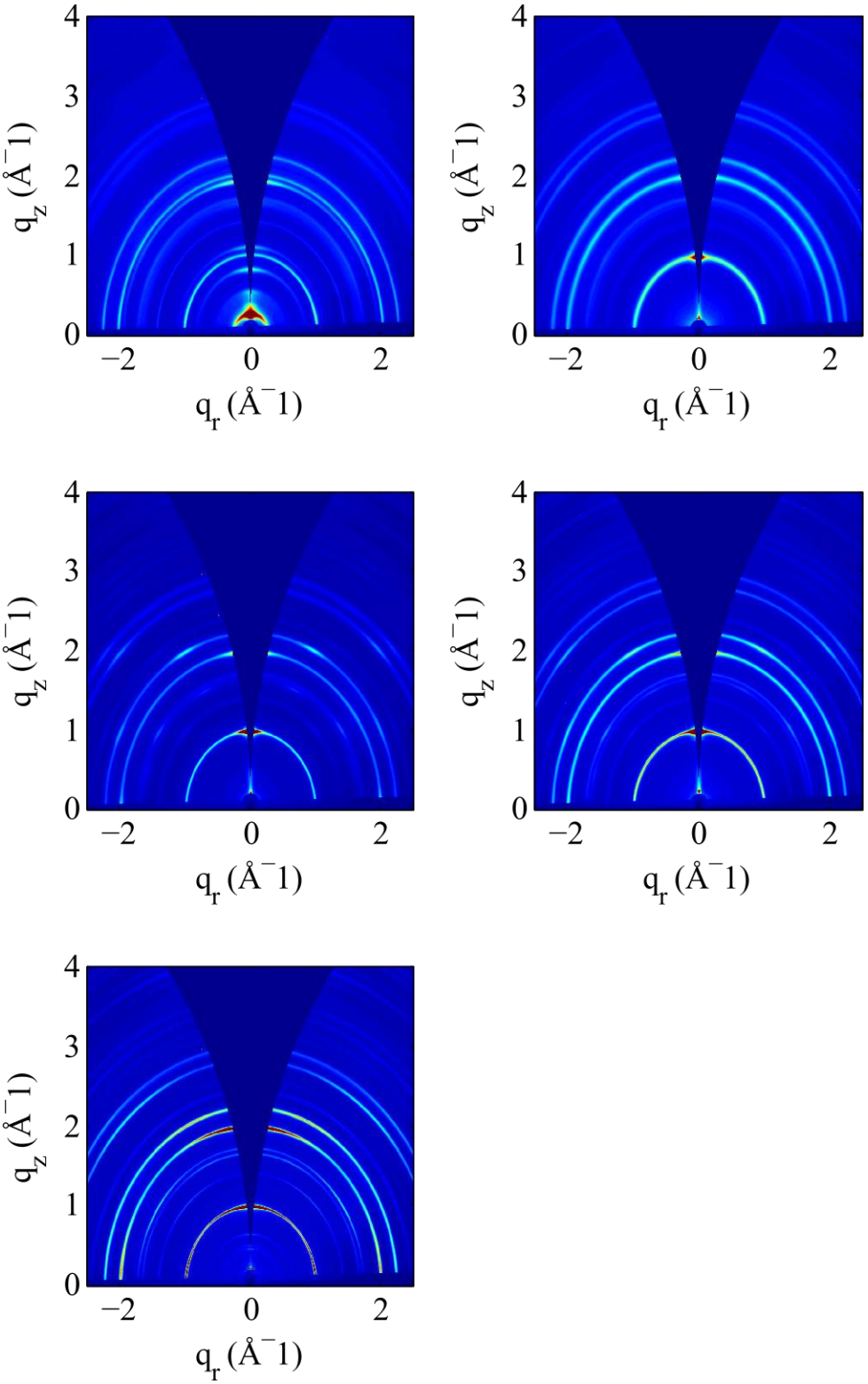


**Figure S25** GIWAXS of samples on Silicon substrate of <n>= 2(a), 5(b), 8(c), 10(d), 40(e).

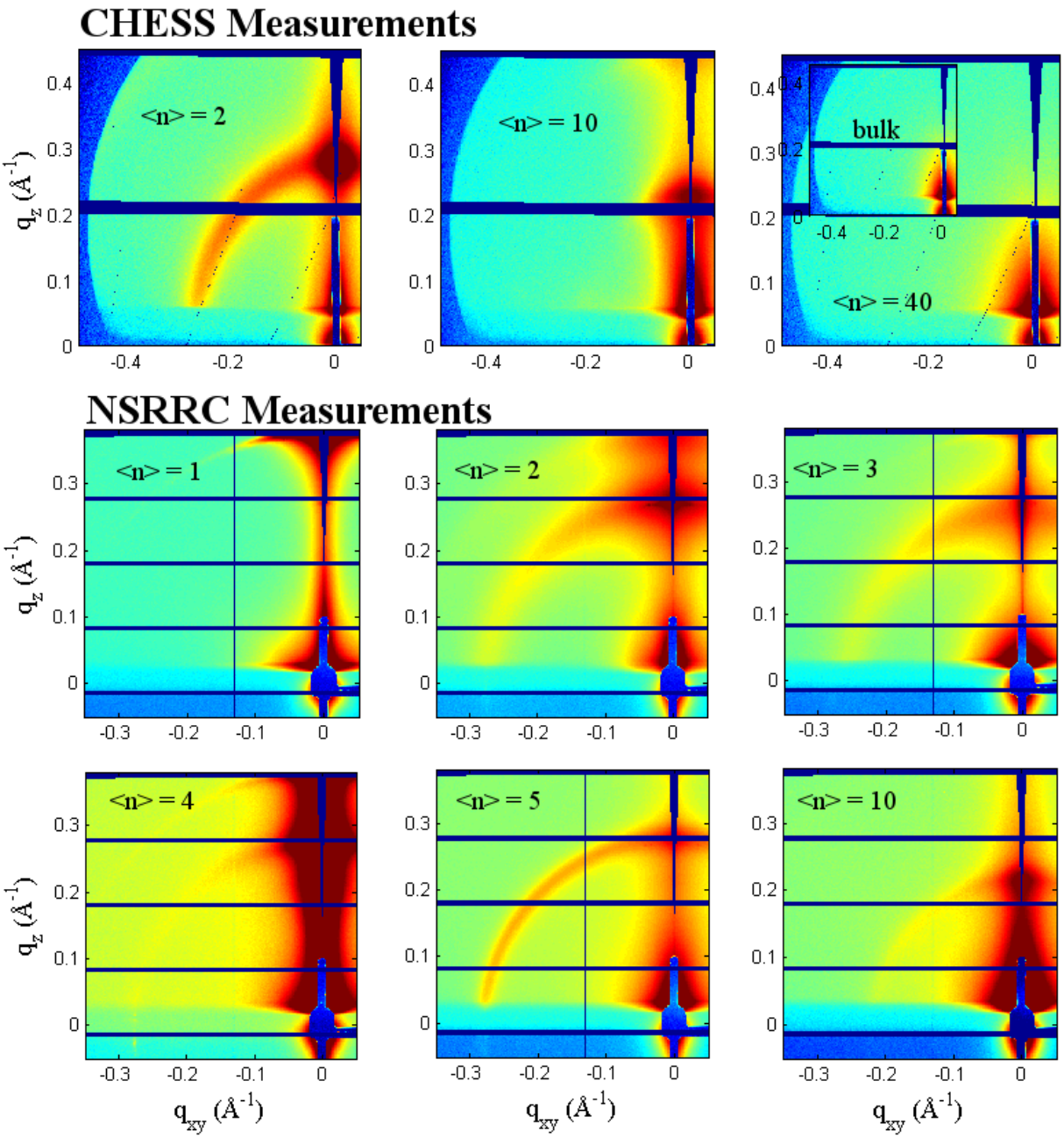


**Figure S26** GISAXS of samples of <n> = 1, 2, 3, 4, 5, 10, 40, and bulk. All are displayed with a log scale for the color axis.

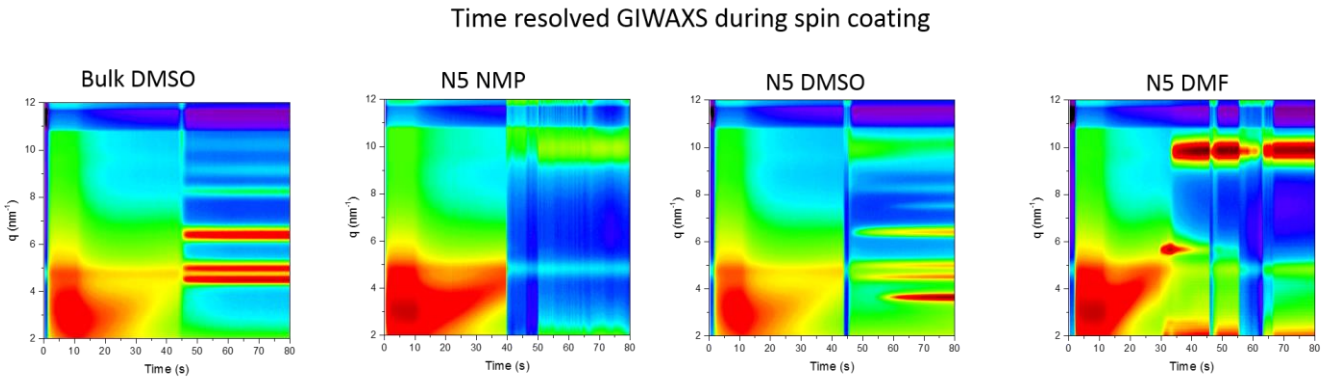


**Figure S27** Time-resolved in-situ GIWAXS measurements performed during spinning integrated for all angles. In all cases, the antisolvent drip occurred at 45 s, except N5 NMP (40 s).

**Table ST2** PL decay lifetimes acquired from bi-exponential fitting of unquenched PEA RDP films, and films with Spiro or PCBM as quenchers. The lifetimes are in turn used to estimate the effective diffusion length of the RDP film as proposed by Lee *et al*[16].

| <n> | Spiro | PCBM | PMMA (Unquenched) | Film Thickness | $L_{diff}$ (PCBM) | $L_{diff}$ (Spiro) | Avg. $L_{diff}$ (nm) |
|---|---|---|---|---|---|---|---|
| 3 | NA | 18.5 ns | 39.9 ns | 190 nm | 184.0729 | NA | 184.0729 |
| 5 | 3.2 ns | 4.9 ns | 23.8 ns | 190 nm | 336.1258 | 434.2377 | 385.1818 |
| 8 | 19.1 ns | 21.2 ns | 99.8 ns | 190 nm | 329.5432 | 351.7945 | 340.6688 |
| 20 | 45.2 ns | 38.3 ns | 207 ns | 190 nm | 359.1924 | 323.8091 | 341.5007 |
| bulk | 18.5 ns | 17.7 ns | 102.8 ns | 190 nm | 375.2728 | 365.3397 | 370.3063 |

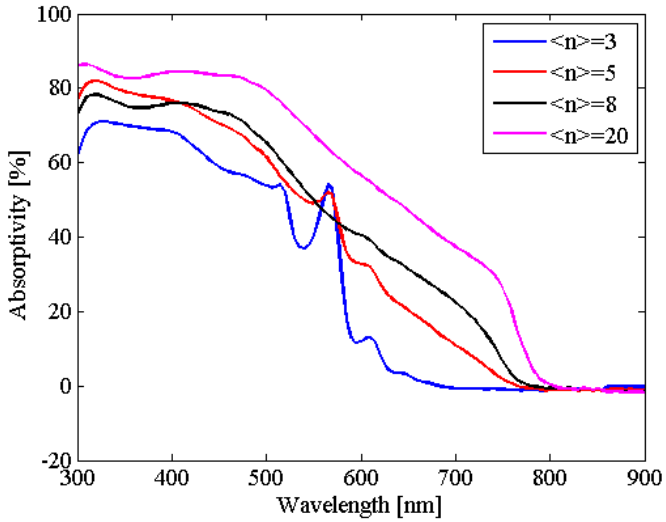


**Figure S28** Absorptivity of RDPs of different <n> values

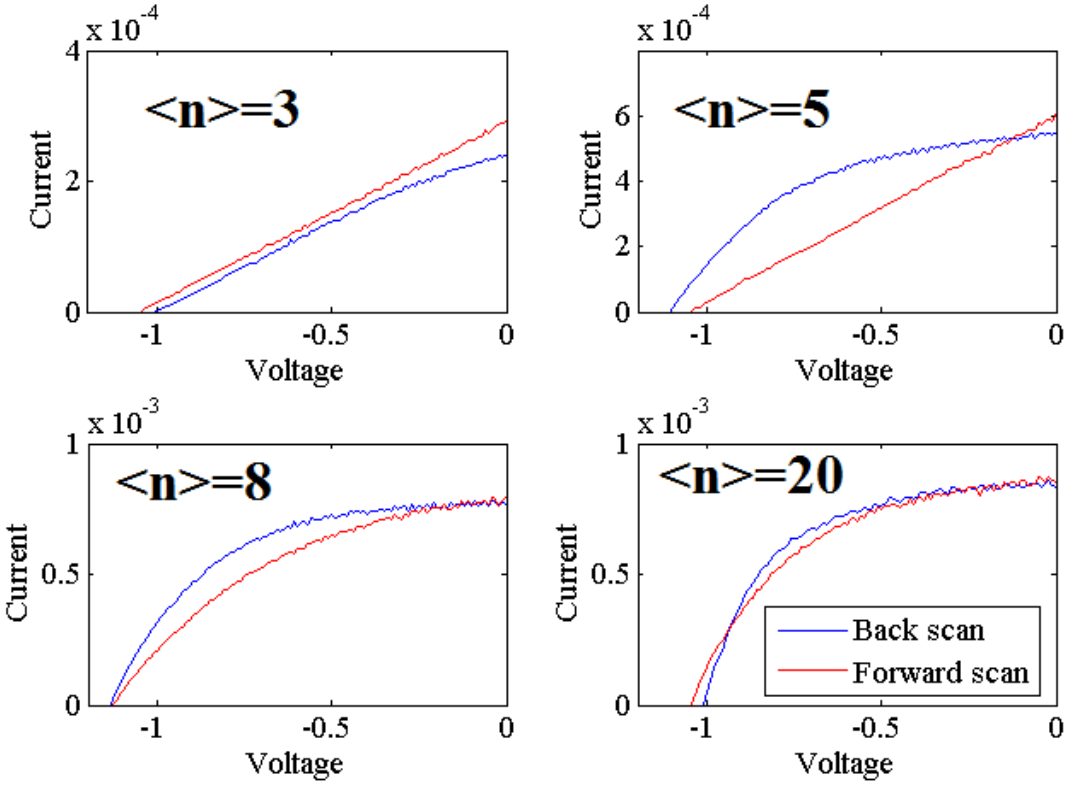


**Figure S29** Hysteresis in PEA RDP films shown in JV curves. Hysteresis in photovoltaic devices is also increased by the introduction of two-dimensional perovskites in PVs. These figures show how the difference between forward and backward JV scans is enhanced as ⟨n⟩ is decreased. This phenomenon could be attributed to the accumulation of charge in RDPs due to imbalanced transport, and also because of thin wells that can act as traps for charge carriers. The band alignment found in previous work[17] suggests that low-n wells would act as shallow traps for holes.

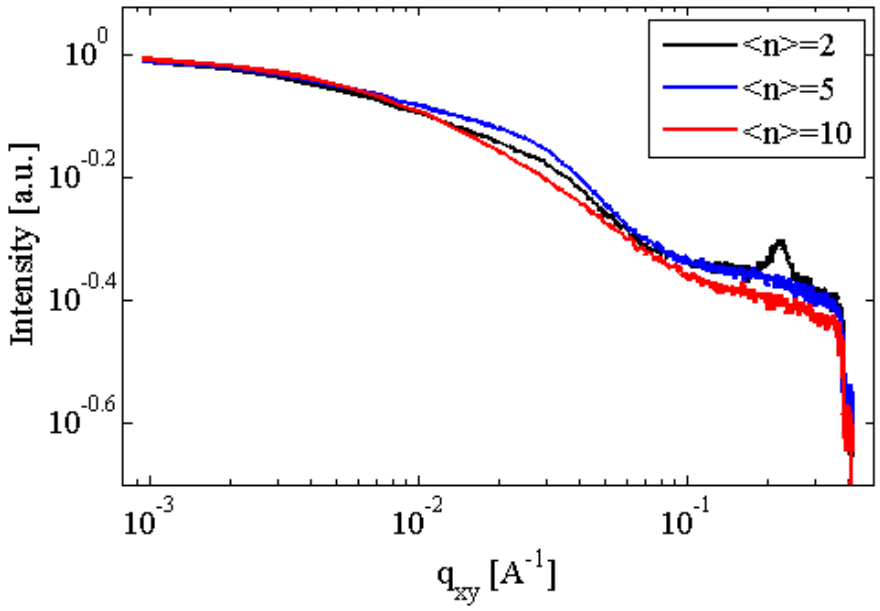


**Figure S30** GISAXS cuts along Qxy.

We have fit the GISAXS data along Qxy to a Unified Model with one level consisting of a Guinier exponential form and a structurally limited power law[18]. In this model, the fitting parameters are:

- G, the exponential scale factor
- Rg, the radius of gyration
- P, the Porod constant
- bg, a constant background

All fits are done from Q=0.03 to Q=0.15 $A^{-1}$. In all fits, the Porod constant tended toward nonphysical values greater than 4, so the value was fixed at 4. The fitted values of the other parameters for <n> = 2,5,10 are displayed below.

| **<n>** | **2** | **5** | **10** |
|---|---|---|---|
| **G** | 0.360 +/- 0.002 | 0.388 +/- 0.002 | 0.367 +/- 0.002 |
| **Rg** | 40.5 +/- 0.2 | 37.7 +/- 0.2 | 39.7 +/- 0.2 |
| **bg** | 0.452 +/- 0.001 | 0.451 +/- 0.001 | 0.429 +/- 0.001 |

Rg describes the length scale of scattering particles, or other contrast in electron density, that leads to the observed SAXS. For all films, the observed Rg is the same length scale of the surface roughness as measured by AFM (Figure S21). Additionally, the contrast between the inorganic perovskite and air is larger than that between the inorganic QWs and the organics. **The measured SAXS likely corresponds to the surface roughness, which prevents any productive interpretation of the model results**.

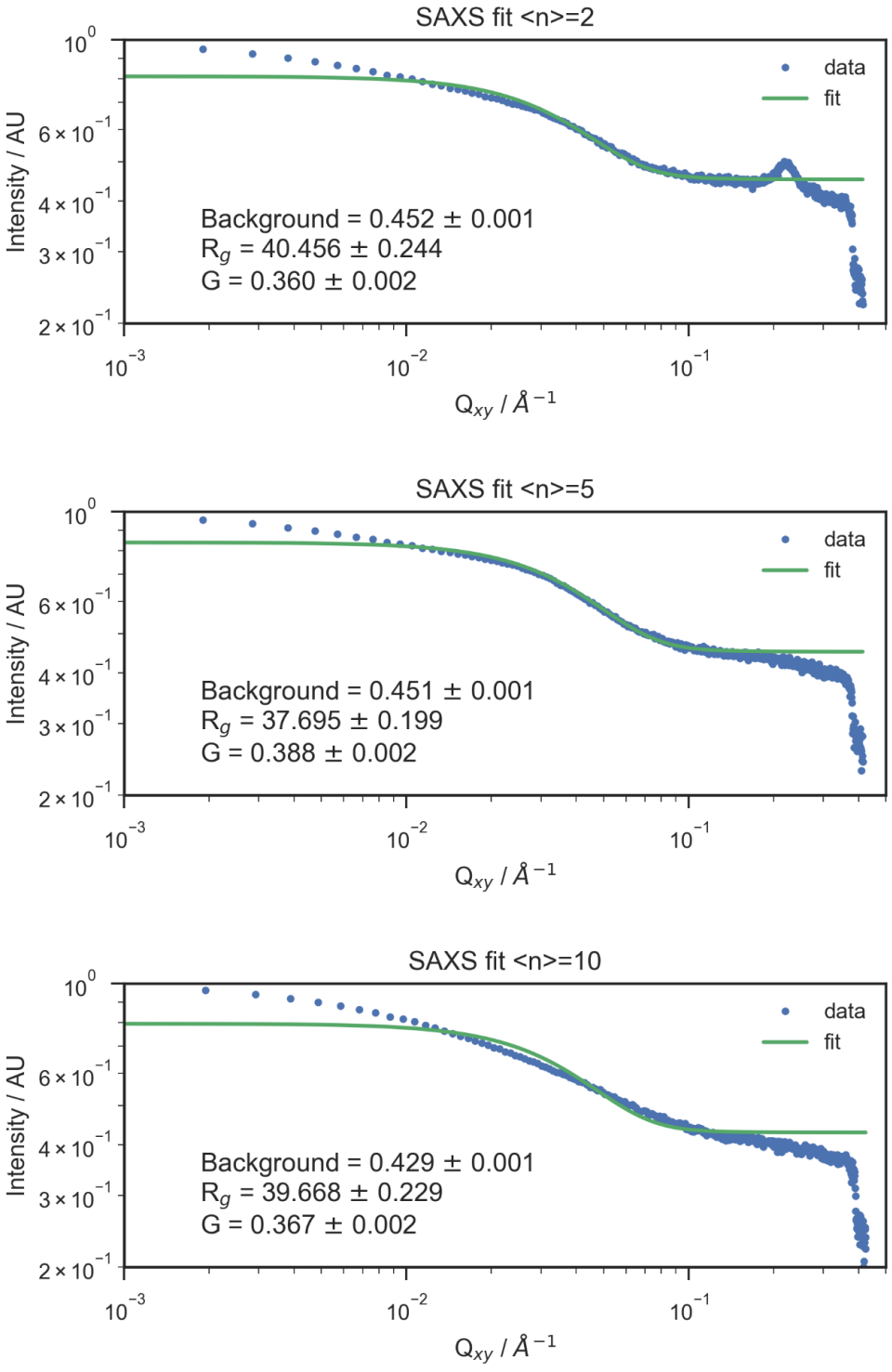


**Figure S31** Fitting of Qxy SAXS cuts (from Figure S30)

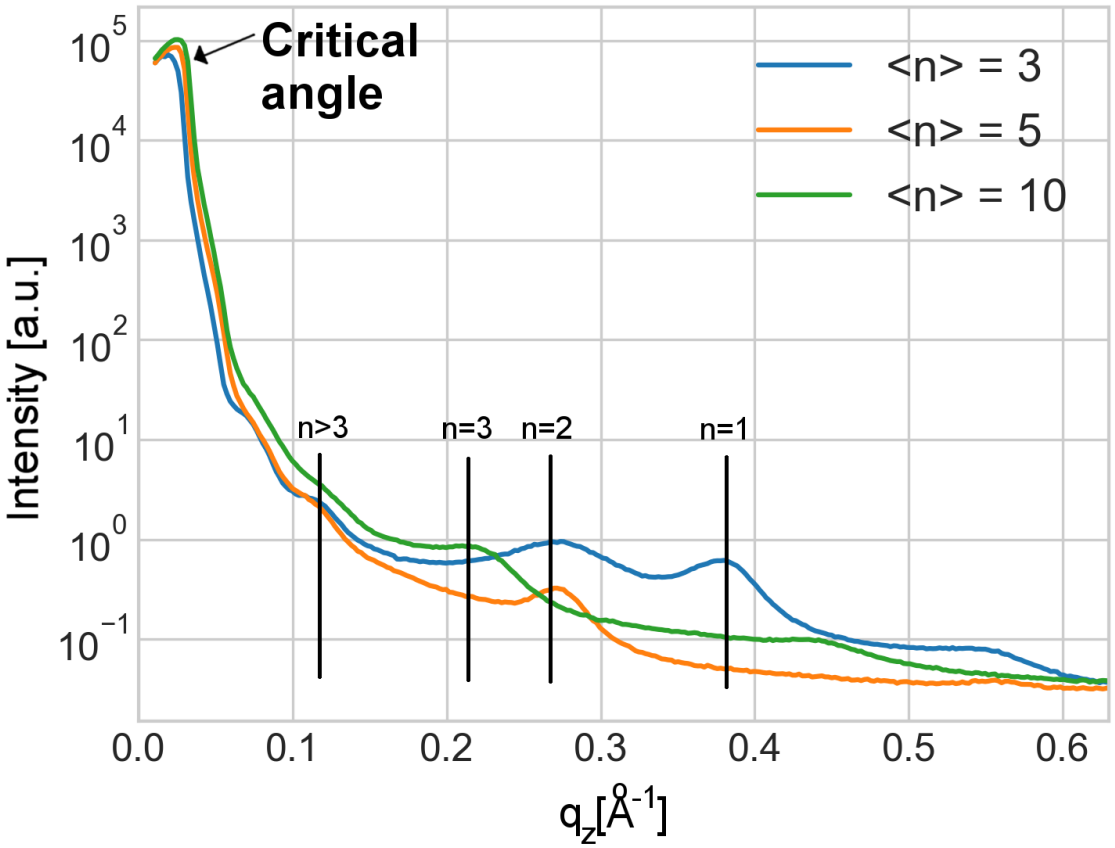


**Figure S32** Low-Qz XRD of RDP films. We observe scattering from total internal reflection below a Qz=0.027, 0.030, and 0.032 for samples <n>=3, 5, and 10, respectively. These correspond to a critical angle of 0.127º, 0.142º, and, 0.151º, respectively. This point was identified as the region where the intensity dropped to 50% of the maximum. The trend exhibited by the samples indicates increasing scattering length density, and therefore increasing physical density as <n> is increased. This can be attributed to a reduction in the proportion of organic ligands and increase in perovskite as <n> is increased.

**Supplementary Videos**

Videos depicting the evolution of the GIWAXS patterns over the course of the annealing process (analyzed in figure 3) are included as supplementary information for the following samples:

- <n>=5 in DMSO
- <n>=10 in DMSO
- <n>=5 in DMF
- <n>=5 in NMP

## References


1. Macrae, C. F. *et al.* Mercury CSD 2.0 - New features for the visualization and investigation of crystal structures. *J. Appl. Crystallogr.* **41,** 466–470 (2008).
2. Momma, K. & Izumi, F. VESTA 3 for three-dimensional visualization of crystal, volumetric and morphology data. *J. Appl. Crystallogr.* **44,** 1272–1276 (2011).
3. Kong, W. *et al.* Characterization of an abnormal photoluminescence behavior upon crystal-phase transition of perovskite CH3NH3PbI3. *Phys. Chem. Chem. Phys.* **17,** 16405–11 (2015).
4. Yamada, Y. *et al.* Dynamic Optical Properties of $CH_3NH_3PbI_3$ Single Crystals As Revealed by One- and Two-Photon Excited Photoluminescence Measurements. *J. Am. Chem. Soc.* **137,** 10456–10459 (2015).
5. Jiang, Z. GIXSGUI: A MATLAB toolbox for grazing-incidence X-ray scattering data visualization and reduction, and indexing of buried three-dimensional periodic nanostructured films. *J. Appl. Crystallogr.* **48,** 917–926 (2015).
6. Patterson, A. L. The scherrer formula for X-ray particle size determination. *Phys. Rev.* **56,** 978–982 (1939).
7. Wu, X., Trinh, M. T. & Zhu, X. Y. Excitonic Many-Body Interactions in Two-Dimensional Lead Iodide Perovskite Quantum Wells. *J. Phys. Chem. C* **119,** 14714–14721 (2015).
8. Leguy, A. M. A. *et al.* Experimental and theoretical optical properties of methylammonium lead halide perovskites. *Nanoscale* **8,** 6317–6327 (2016).
9. Liu, J., Leng, J., Wu, K., Zhang, J. & Jin, S. Observation of Internal Photoinduced Electron and Hole Separation in Hybrid 2-Dimentional Perovskite Films. *J. Am. Chem. Soc.* **139,** 1432–1435 (2017).
10. Moreels, I. *et al.* Size-dependent optical properties of colloidal PbS quantum dots. *ACS Nano* **3,** 3023–3030 (2009).
11. Wang, Y., Suna, A., Mahler, W. & Kasowski, R. PbS in polymers. From molecules to bulk solids. *J. Chem. Phys.* **87,** 7315–7322 (1987).
12. Ma, J. & Wang, L. Nanoscale Charge Localization Induced by Random Orientations of Organic Molecules in Hybrid Perovskite CH 3 NH 3 PbI 3. *Nano Lett.* **15,** 248–253 (2014).
13. Yang, Y. *et al.* Observation of a hot-phonon bottleneck in lead-iodide perovskites. *Nat. Photonics* **10,** 53–59 (2015).
14. Yang, J. P. *et al.* What determines the lamellar orientation on substrates? *Macromolecules* **44,** 3511–3516 (2011).
15. Busch, P. *et al.* Lamellar Diblock Copolymer Thin Films Investigated by Tapping Mode

Atomic Force Microscopy:Â Molar-Mass Dependence of Surface Ordering. *Macromolecules* **36,** 8717–8727 (2003).

16. Lee, E. M. Y. & Tisdale, W. A. Determination of exciton diffusion length by transient photoluminescence quenching and its application to quantum dot films. *J. Phys. Chem. C* **119,** 9005–9015 (2015).

17. Cao, D. H., Stoumpos, C. C., Farha, O. K., Hupp, J. T. & Kanatzidis, M. G. 2D Homologous Perovskites as Light-Absorbing Materials for Solar Cell Applications. *J. Am. Chem. Soc.* **137,** 7843–7850 (2015).

18. Ilavsky, J. & Jemian, P. R. Irena: Tool suite for modeling and analysis of small-angle scattering. *J. Appl. Crystallogr.* **42,** 347–353 (2009).